

TORQUE PROFILE IMPROVEMENT OF DOUBLE STATOR
SWITCHED RELUCTANCE MOTOR THROUGH MECHANICAL
OFFSET BETWEEN INNER AND OUTER STATOR

by

Colbey N. Hair

APPROVED BY SUPERVISORY COMMITTEE:

Babak Fahimi, Chair

Matthew Gardner

Poras T. Balsara

Copyright © 2020

Colbey N. Hair

All rights reserved

TORQUE PROFILE IMPROVEMENT OF DOUBLE STATOR
SWITCHED RELUCTANCE MOTOR THROUGH MECHANICAL
OFFSET BETWEEN INNER AND OUTER STATOR

by

COLBEY N. HAIR, BS

THESIS

Presented to the Faculty of
The University of Texas at Dallas
in Partial Fulfillment
of the Requirements
for the Degree of

MASTER OF SCIENCE IN
ELECTRICAL ENGINEERING

THE UNIVERSITY OF TEXAS AT DALLAS

December 2020

ACKNOWLEDGMENTS

This thesis would not have been possible without the support from many people at the REVT lab. Thank you to Tianyu Chen for his help with the firmware, to Carlos Caicedo for help with constructing a useful test fixture, to Jingchen Liang and Amir Parsapour for patient and extended extended support on the magnetic simulations, and to Mehdi Moallem and Ion Boldea for their mentorship on the analytic and magnetic aspects. I also extend a large thanks to my advisor, Babak Fahimi, for providing the funding and lab space to enable this thesis, as well as his generous and consistent time commitment for mentorship and to ensure I had all investigation needs met.

November 2020

TORQUE PROFILE IMPROVEMENT OF DOUBLE STATOR
SWITCHED RELUCTANCE MOTOR THROUGH MECHANICAL
OFFSET BETWEEN INNER AND OUTER STATOR

Colbey N. Hair, MS
The University of Texas at Dallas, 2020

Supervising Professor: Babak Fahimi, Chair

The double stator switched reluctance motor is a derivative of the traditional SRM, using a segmented rotor and two coaxial stators to increase flux density in the machine and improve torque density. Switched reluctance motors suffer from a propensity to high torque ripple, and the DSSRM inherits this shortcoming. This work investigates a method to reduce torque ripple in the DSSRM by strategically misaligning the two stators, which are aligned in the nominal design. The methods for simulation and data postprocessing will be discussed, as well as a discussion of the mechanism for reduced torque ripple.

TABLE OF CONTENTS

| | |
|---|------|
| ACKNOWLEDGMENTS | iv |
| ABSTRACT | v |
| LIST OF FIGURES | viii |
| LIST OF TABLES | xi |
| CHAPTER 1 INTRODUCTION | 1 |
| 1.1 The switched reluctance motor | 1 |
| 1.2 The double-stator switched reluctance machine | 3 |
| 1.3 Torque ripple | 4 |
| 1.4 History | 5 |
| 1.5 Energy conversion basics | 7 |
| 1.6 Nonlinear energy conversion | 13 |
| 1.7 Linear model of the SRM | 15 |
| 1.8 Other investigations | 20 |
| CHAPTER 2 NUMERICAL ANALYSIS | 22 |
| 2.1 Simulation | 22 |
| 2.1.1 Physical setup | 22 |
| 2.1.2 Electrical setup | 24 |
| 2.1.3 Motion setup | 24 |
| 2.1.4 Transient setup | 24 |
| 2.1.5 Input parameters | 25 |
| 2.1.6 Output data | 26 |
| 2.2 Data analysis | 27 |
| 2.2.1 Objective function | 28 |
| 2.3 Optimization results | 30 |
| CHAPTER 3 EXPERIMENTAL VALIDATION | 34 |
| 3.1 Test platform hardware | 34 |
| 3.2 Inverter software | 37 |
| 3.2.1 Periodic task management | 37 |

| | | |
|--|---|----|
| 3.2.2 | Current sensing | 38 |
| 3.2.3 | Current control | 38 |
| 3.2.4 | Position and speed monitoring | 40 |
| 3.2.5 | Fault detection | 40 |
| 3.2.6 | Speed control | 40 |
| 3.2.7 | Current commutation | 41 |
| 3.2.8 | Control block digram | 41 |
| 3.2.9 | Analog feedback | 41 |
| 3.3 | Experimental measurements | 42 |
| 3.3.1 | Static torque profile | 42 |
| 3.3.2 | Commutated torque profile | 43 |
| 3.3.3 | Inductance profiles | 44 |
| 3.4 | Experimental results | 44 |
| CHAPTER 4 MECHANISM FOR TORQUE PROFILE IMPROVEMENT | | 47 |
| 4.1 | Harmonic analysis of torque profile | 47 |
| 4.2 | Back emf analysis | 49 |
| 4.3 | Inductance torque contributions | 55 |
| CHAPTER 5 CONCLUSION | | 60 |
| 5.1 | Future work | 60 |
| REFERENCES | | 62 |
| BIOGRAPHICAL SKETCH | | 64 |
| CURRICULUM VITAE | | |

LIST OF FIGURES

| | | |
|------|---|----|
| 1.1 | Flux path of the DSSRM. The flux path nominally links only one stator and does not travel through the rotor into the opposite stator. This illustration ©2019 IEEE (Hair et al., 2019) | 4 |
| 1.2 | Cross-sectional view of a solenoid. The current flowing through the wires creates a magnetic field as shown. The grey box is a steel plunger which can translate left and right. | 8 |
| 1.3 | Magnetization curves with plunger removed (vacuum) and with plunger inserted (steel). The aligned and unaligned position are terms used in a rotary system, discussed in section 1.7 | 10 |
| 1.4 | Evolution of the potential energy in a linear system as the movable element translates through an infinitesimal displacement $d\theta$. The change in potential energy of the system is shown as the shaded area between the curves. | 11 |
| 1.5 | Magnetization curve for a system in a high permeability configuration (steel or aligned) and in a low permeability configuration (vacuum or unaligned). | 13 |
| 1.6 | Differential change in potential energy as the system evolves from the empty (vacuum or unaligned) to full (steel or aligned) configurations. | 14 |
| 1.7 | Physical model of a theoretical SRM, shown in the aligned position for phase A. | 16 |
| 1.8 | Switched reluctance motor shown in the unaligned position for phase A | 16 |
| 1.9 | Flux path through the SRM in the aligned position, with phase A active. | 17 |
| 1.10 | Equivalent magnetic circuit of the SRM showing all airgap reluctances and all phase windings | 18 |
| 1.11 | Simplified magnetic equivalent circuit used to describe the flux through the motor with single-phase excitation. | 18 |
| 2.1 | Physical model of the DSSRM | 23 |
| 2.2 | Motion band for the DSSRM. All objects inside the highlighted ring move at constant angular velocity. | 25 |
| 2.3 | Static torque profiles from the motor with some arbitrary stator offsets. | 26 |
| 2.4 | Commutated torque profile and the corresponding static torque profile used to derive it. | 28 |
| 2.5 | Commutated torque profile with the correct firing angle and an arbitrarily selected incorrect firing angle. | 30 |
| 2.6 | Performance metrics vs stator offset for two-phase operation of the motor. | 31 |

| | | |
|-----|--|----|
| 2.7 | Nominal vs optimal torque profiles of the motor operated in two-phase mode. The red line represents the commutated and static torque profile of the original motor, while the black line represents the commutated and static torque profile of the optimized motor. | 31 |
| 2.8 | Performance metrics vs stator offset for single-phase operation of the motor. . . | 32 |
| 2.9 | Nominal vs optimal torque profiles of the motor operated in single-phase mode. The red line represents the commutated and static torque profile of the original motor, while the black line represents the commutated and static torque profile of the optimized motor. | 32 |
| 3.1 | Test platform used for evaluating the DSSRM. Not shown are the high voltage power supply and electronic load. This illustration ©2019 IEEE (Hair et al., 2019) | 35 |
| 3.2 | Control block diagram used to operate the DSSRM. | 42 |
| 3.3 | Static torque profile of the motor under two-phase excitation. The red dashed line is the torque from the nominal motor, and the solid red line is the torque from the optimized motor. This illustration ©2019 IEEE (Hair et al., 2019) . . | 45 |
| 3.4 | Commutated torque profile of the motor under two-phase excitation. The red dashed line is the torque from the nominal motor, and the solid red line is the torque from the optimized motor. This illustration ©2019 IEEE (Hair et al., 2019) | 45 |
| 3.5 | Inductance of phase A in the DSSRM for nominal and offset conditions. The top pane shows the predicted inductance from simulation, while the lower pane shows inductance measured experimentally as described in section 3.3.3. This illustration ©2019 IEEE (Hair et al., 2019) | 46 |
| 4.1 | Model for interpreting harmonic content of torque profile. Each stator provides a torque contribution, and the sum is observed at the shaft. | 48 |
| 4.2 | Estimated torque components from the back emf on the inner and outer stator for static excitation on phase A, in the aligned stator configuration. Note that the peaks in torque from the inner and outer stator are well aligned. | 50 |
| 4.3 | Estimated torque components from the back emf on the inner and outer stator for static excitation on phase A, in the offset stator configuration. Note the offset between the peaks of the torque contributions from each stator. | 50 |
| 4.4 | Estimated torque components from the back emf on the inner and outer stator for static excitation on phase A and B, in the aligned stator configuration. . . . | 51 |
| 4.5 | Estimated torque components from the back emf on the inner and outer stator for static excitation on phase A and B, in the offset stator configuration. | 52 |
| 4.6 | Static torque profile contributions from the inner and outer stator for single-phase excitations. The solid line is the torque estimate, while the dashed line represents a first-order Fourier series representation. The vertical bars represent the peaks of the sine fit. | 52 |

| | | |
|------|--|----|
| 4.7 | Commutated torque profile contributions from the inner and outer stator for single-phase excitations. The solid line is the torque estimate, while the dashed line represents a sine wave fit to the torque estimate. The vertical bars represent the peaks of the sine fit. | 53 |
| 4.8 | Static torque profile contributions from the inner and outer stator for two-phase excitations. The solid line is the torque estimate, while the dashed line represents a first-order Fourier series representation. The vertical bars represent the peaks of the sine fit | 54 |
| 4.9 | Commutated torque profile contributions from the inner and outer stator for two-phase excitations. The solid line is the torque estimate, while the dashed line represents a sine wave fit to the torque estimate. The vertical bars represent the peaks of the sine fit. | 55 |
| 4.10 | Torque contributions from the inductance matrix of the motor in single-phase mode. Green regions represent regions where the torque after optimization is greater than the original torque. | 57 |
| 4.11 | Torque contributions from the inductance matrix of the motor in two-phase mode. Green regions represent regions where the torque after optimization is greater than the original torque. | 59 |

LIST OF TABLES

| | |
|----------------------------------|----|
| 2.1 Machine Parameters | 33 |
|----------------------------------|----|

CHAPTER 1

INTRODUCTION

The double stator switched reluctance motor (DSSRM) is a variant of the traditional switched reluctance motor (SRM), with the addition of a second stator, so that two stators are acting on the same rotor. The DSSRM offers better torque density than the SRM, although it inherits the issue of large torque ripple. This work aims to answer one question: can the torque ripple be reduced in the DSSRM by intentionally misaligning the two stators, without penalizing mean torque excessively?

This chapter will start with an overview of the SRM and DSSRM. A brief history will be discussed, then the chapter will conclude with a brief overview of energy conversion principles in switched reluctance machines.

1.1 The switched reluctance motor

The switched reluctance motor (SRM) is a type of electric machine which produces torque without permanent magnets and a rotor which is constructed of magnetic steel pressed onto a shaft. The motor is simple and inexpensive to manufacture, offers extremely good tolerance for thermal extremes, and can operate at very high speeds. The SRM cannot be operated without an inverter, and as such is suitable for any application which requires variable speed drives, although for fixed speed operation the inverterless AC induction motor is still cheaper. Regarding volumetric and gravimetric torque density, the singly-excited induction motor and the SRM are approximately matched (Maharjan et al., 2018).

The operation of a switched reluctance motor is easily described as an electromagnet attracting a piece of steel. A traditional SRM rotor has several "cog" features protruding from its surface. The stator contains several corresponding cogs which house concentrated coils. When a current flows in the phase winding, the stator becomes an electromagnet which

attracts the nearest rotor tooth. The rotor will then move to align itself with the energized phase, but as the rotor approaches alignment, that stator winding is deactivated and the subsequent winding is activated. By commutating the stator currents in this way, the rotor will experience a continuous, positive torque which is useful for doing work, although this discontinuous, nonlinear torque production mechanism leads to large torque ripple, one of the fundamental shortcomings of the motor family.

The switched reluctance motor can operate at extreme temperatures which would stress other types of motors, namely permanent magnet motors. Motors which use neodymium magnets must operate within a tight temperature band to avoid demagnetization. Most frequently, the magnets are mounted to the rotor which compounds the cooling challenges greater. The SRM can easily operate at any high temperature so long as the core material stays below its annealing and curie temperatures and the conductor insulation is not degraded. Permanent magnet motors using the appropriate formulation of neodymium magnet can be operated in the range of $[-40,150]$ C, although the torque of the motor may be derated as much as 15% at high temperatures (Sebastian, 1995). Switched reluctance motors can easily be designed in a range of $[-200,500]$ C, with one design for a high temperature switched reluctance generator described in (Richter, 1988) and a design for a switched reluctance motor operated in liquid nitrogen described in (Brown et al., 2007).

The switched reluctance motor is also well-suited to high speed operation. Perhaps most notably, the rotor in a switched reluctance motor is often nothing more than laminated steel pressed onto a steel shaft, which results in a mechanically robust structure capable of withstanding the stresses from high speed rotation. In contrast, surface mounted permanent magnets may dislodge from the rotor surface. Similarly, rotor windings in an induction or DC motor can fly outwards causing a “bird’s nest” failure at high speed. An overview of motors suited for high speed operation is explored thoroughly in (Rahman et al., 2004).

1.2 The double-stator switched reluctance machine

The double stator switched reluctance machine (DSSRM) is a switched reluctance motor which contains more than one stator that both act on a single rotor. The DSSRM is realized in many forms, including axial-flux, radial-flux, and linear machines. Among these, the machines can be further categorized by their flux path, with some machines generating a flux that links both stators, and some machines creating flux that links only one stator. The DSSRM in this work is a radial-flux machine with a flux path that nominally links only one stator, as illustrated in Fig. 1.1. In this work, the term DSSRM will refer to such a configuration, while machines with other configurations will be specified as such.

The motivation for the DSSRM is primarily to improve the torque density of the SRM. Upon inspection of the microscopic forces inside the single stator SRM, it has been shown (Abbasian et al., 2010) that the radial forces on the rotor are significantly higher than the tangential forces. In a SRM, the goal is to produce as much torque on the rotor as possible, and tangential magnetic forces are the only forces which do so. Radial forces will attract the stator poles to the rotor poles and vice versa, which does not produce any torque, and even produces deflection in both bodies, leading to vibration and acoustic noise. By placing a stator on both sides of a rotor segment, the magnetic scalar potential is balanced in the radial direction, and maximized in the tangential direction, leading to much greater tangential forces. The ratio of tangential to radial forces can indicate the torque production efficiency of a machine; in the DSSRM this ratio can be 5 times greater than in the SRM.

Although the DSSRM has an improved torque density, the configuration of the motor leads to special challenges in manufacturing and operation. The mechanical resilience of the rotor is diminished greatly with its cylindrical shape, which will deflect much more radially at high speed compared with the solid rotor in an SRM. The rotor cage also presents a loss mechanism if the material is conductive; the rotor cage in the prototype of this work is made from aluminum, which will lead to significant eddy current losses from moving in the

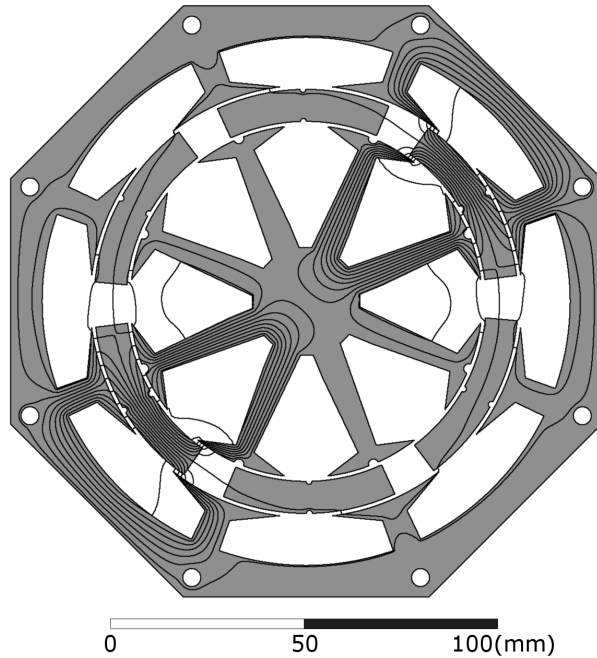


Figure 1.1. Flux path of the DSSRM. The flux path nominally links only one stator and does not travel through the rotor into the opposite stator. This illustration ©2019 IEEE (Hair et al., 2019)

magnetic field. In the coaxial two-stator configuration, the inner stator is inherently difficult to access and is accordingly more difficult to cool. These effects have been explored in great detail for the development of a 100kW DSSRM prototype in (Maharjan et al., 2018).

1.3 Torque ripple

Due to the step-wise operation of the SRM, the torque output is far from uniform. The torque produced by the motor while a phase is first activated may be very different from the torque produced near the end of the phase activation. This nonuniformity of the torque is called the torque ripple, and is typically represented as the ratio of torque variation to average torque. The DSSRM inherits this shortcoming from the SRM. A rigorous definition of torque ripple is given in Chapter 2.

1.4 History

The switched reluctance motor is one of the simplest forms of electric machine, and it represents the culmination of over 100 years of engineering evolution. Early electric machines were often constructed primarily for demonstration purposes, although the patents showed a more optimistic view of the applications of such machines. Many such machines did not employ continuous rotary motion, such as the Page's motor in 1844, which was essentially a reciprocating engine having a magnetic solenoid substituted for a pneumatic piston (Miller, 2001). Many other engines from this era used linear magnetic actions and some type of crank mechanism to create continuous rotary motion.

A notable development in electric machines came from synchronous reluctance motors, in which the magnetic action was directly integrated into the rotary motion, creating the first reluctance motors which resemble the modern cylindrical motors of today. One such example is Bouchot's synchronous machine in 1908, intended to run directly from an AC mains source (Miller, 2001). This motor, as with any synchronous motor, required that the rotor and the AC power source be perfectly synchronized in order to create usable torque. In the modern day, adjustable speed drives synchronize the power source to the rotor, but before inverters were ubiquitous, the rotor had to be aligned with the AC grid instead. This led to limits in the application of synchronous machines due to the extra complexity of bringing the motor to synchronization before energizing its windings.

Although the switched reluctance motor had the advantage of early development, it was eclipsed by the rapid development of two alternative motor topologies. The brushed DC motor was an efficient machine for use on DC sources such as batteries or the DC electric grid available in some cities in the 1880s (Carlson, 2013). Nikola Tesla's AC induction motor was useful for AC sources, such as the AC grid that became the global standard after 1893 when Westinghouse was awarded the Niagara Falls hydroelectric generation project (Carlson, 2013).

Both the brushed DC motor (BRDC) and induction AC motor (IM) provided the immediate benefit of simplicity in operation and control. Each of these motors is an asynchronous machine, which allows operation over a range of speeds, as well as easy starting by connecting them directly to a power source even if the motor is at zero speed. Larger motors would use starters, but this was typically a simple device such as a resistor bank that would limit the starting current to avoid damaging transients at very low speed.

The IM uses a rotating magnetic field to induce currents in a rotor, which themselves create a force in opposition to the original field from the stator. The reaction between these two currents creates a continuous torque. The BRDC has windings on the rotor and windings or permanent magnets on the stator, and the current in the rotor windings is commutated by means of a mechanical brush assembly, called the commutator. In effect, the BRDC is also an AC motor if the current is observed in an arbitrary rotor winding, and the brushed commutator is an early, rudimentary, and mechanical form of an inverter, creating an AC current in the rotor.

Both the IM and BRDC became the dominant form of energy conversion in the early 1900s, superseding the switched reluctance motor which was limited by the lack of efficient or reliable inverter drives. Before electronic switches and semiconductors, power was controlled with mechanical switches. In the BRDC, the mechanical brush system works well because the phase current is near zero at the moment of commutation, and any remaining current is shunted into the subsequent coil. In a switched reluctance motor, which is effectively a collection of solenoids, the current has no such zero crossing, and breaking a current will create arcing. The switched reluctance motor operates by briefly storing energy in a magnetic field in the phase windings, then removing that energy at the correct time; if the current is commutated with a mechanical switch, the energy will mostly be dissipated in the switch as an arc, which results in significant wasted energy and rapid wear on the switch device.

Solid state switching devices provided the current control required for efficient and reliable operation of switched reluctance motors. Although rudimentary forms of current control

existed in the 1930s, such as the mercury arc thyristor, truly practical power electronics were not available until the 1960s with the thyristor (Miller, 2001). The thyristor was capable of switching very high voltages and reasonable currents, but it suffered from the limitation that, once turned on, the switch could not be turned off until the device current reaches a zero crossing, as happens in a bridge rectifier. The power MOSFET became viable in the 1970s due to its superior switching speed and controllability over the thyristor, but was itself superseded by the IGBT in the 1980s which offered better efficiency in high current applications. Today, the MOSFET and IGBT are the most common switches in industry, with the MOSFET offering better performance in high frequency applications due to fast turn-off, and the IGBT offering better efficiency in high current applications, with lower voltage drop than MOSFETs at high currents (Iwamuro and Laska, 2017).

While semiconductor switches allowed for reliable and efficient control of current in a SRM, the devices used for controlling the motor drive went through a similar evolutionary process. Early motor drives were only available with analog control circuitry until the mid 1980s, when microcontrollers became sufficiently cheap and powerful to execute digital control algorithms. The switched reluctance motor can be operated using very simple control algorithms, but some adaptive controls such as sensorless operation present significant complication when realized in analog form. The digital control of motors is dominant today due to the low cost of microcontroller hardware as well as the rapid adaptability of digital control algorithms.

1.5 Energy conversion basics

Consider a linear magnetic device: a solenoid, illustrated in Fig. 1.2. The solenoid consists of a cylindrical coil of wire with a void in the center, into which a steel plunger may be inserted. When a current is injected into the solenoid, a magnetic field will form. While the solenoid is empty, a very small flux will form due to the low permeability of air, but as

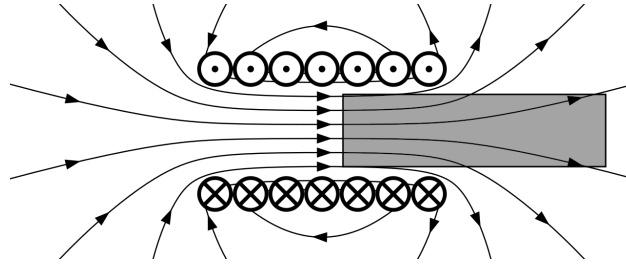


Figure 1.2. Cross-sectional view of a solenoid. The current flowing through the wires creates a magnetic field as shown. The grey box is a steel plunger which can translate left and right.

the plunger enters the solenoid, the flux will increase significantly due to the relatively high permeability of steel. The relationship between current, flux, magnetic energy, and force on the plunger will be derived. Note that this example is somewhat simplified by neglecting the reluctance of the flux return path from one side of the solenoid to the other; rather than perfect fidelity, this model is intended to provide intuition.

The magnetic field in the solenoid is given by

$$B = \mu H \quad (1.1)$$

The flux linkage in this solenoid is

$$\lambda = N\phi = N \frac{f}{R} = \frac{N^2 i}{R} \quad (1.2)$$

where N is the number of turns of wire in the solenoid and R is the reluctance, or the magnetic equivalent of resistance. Using the definition of reluctance, eq. 1.2 becomes

$$\lambda = \frac{N^2 i}{\frac{l}{\mu A}} = \frac{N^2 A i}{l} \mu \quad (1.3)$$

where μ is a simplified combination of the permeability of vacuum and plunger, depending how far the plunger is inserted.

It is convenient to define a quantity that relates the flux linkage with current. This quantity is called inductance, defined in eq. 1.4. When a magnetic circuit is called linear,

that indicates that the inductance value is constant, and thus the relationship between flux linkage and current is linear. Inductance can be defined as apparent inductance, relating the total flux to the total current, or the incremental inductance, relating the infinitesimal change in flux to the infinitesimal change in current. For a linear device, these values are identical, although this is not the case for a saturated machine as discussed later.

$$L = \frac{\lambda}{i} = \frac{d\lambda}{di} = \frac{N^2}{R} = \frac{N^2 A}{l} \mu \quad (1.4)$$

The force on the solenoid can be described in terms of the potential energy gradient of the system in eq. 1.5. Note that a solenoid has only one degree of freedom, which reduces it to a one-dimensional system. To put eq. 1.5 into words, the force on the plunger as it is inserted into the solenoid depends on how quickly the potential energy of the system changes with plunger position.

$$F = -\nabla W = -\frac{\partial W}{\partial x} \quad (1.5)$$

For simplicity, only the magnitude of force will be considered and the negative sign is dropped. To find the force, the energy must be described. Consider the terminal equations of the solenoid in eq. 1.6. The voltage is the sum of the voltage drop from the resistance in the coil and back emf ε from Faraday's law of induction.

$$v = Ri + \varepsilon = Ri + \frac{d\lambda}{dt} = Ri + i \frac{dL}{dt} + L \frac{di}{dt} \quad (1.6)$$

For simplicity, the resistance will be neglected as a non-conservative phenomenon. The potential energy W in this system is derived as

$$W = \int_0^{T_1} i(t) v(t) dt = \int_0^{T_1} i \frac{d\lambda}{dt} dt = \int_0^{\lambda_1} i d\lambda \quad (1.7)$$

Substituting eq. 1.7 into eq. 1.5 yields

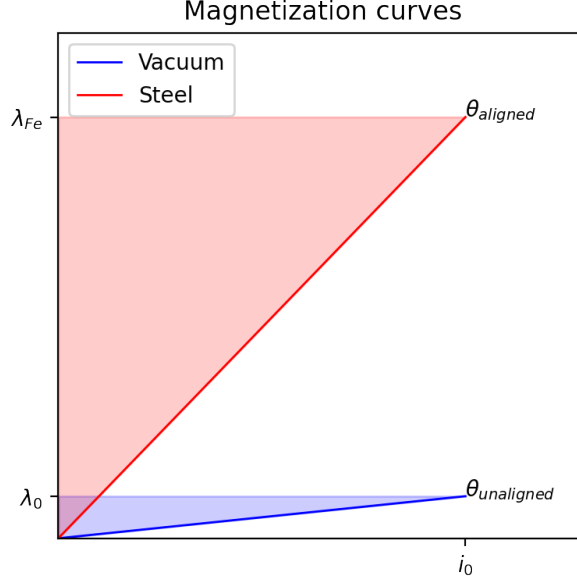


Figure 1.3. Magnetization curves with plunger removed (vacuum) and with plunger inserted (steel). The aligned and unaligned position are terms used in a rotary system, discussed in section 1.7

$$F = \frac{\partial W}{\partial x} = \frac{\partial}{\partial x} \int_0^{\lambda_1} i d\lambda \quad (1.8)$$

Consider the magnetization curve for the solenoid with the plunger removed, the blue line in Fig. 1.3. The blue shaded region represents the energy required to magnetize the system in the empty configuration, and it has area of $i\lambda - \frac{1}{2}iN\mu_0$.

If the plunger is inserted completely into the solenoid, the permeability of the magnetic circuit increases, the reluctance decreases, and much more flux flows for the same current, shown with the red line in Fig. 1.3. The red shaded area is now $i\lambda - \frac{1}{2}iN\mu$, using μ for the steel rather than μ_0 for a vacuum.

As the plunger is inserted an infinitesimal distance dx (or as illustrated, $d\theta$), the infinitesimal change in potential energy dW is proportional to the area between the two curves in Fig. 1.4. For nonzero solenoid current, the plunger will experience a force that tends to pull it into the solenoid.

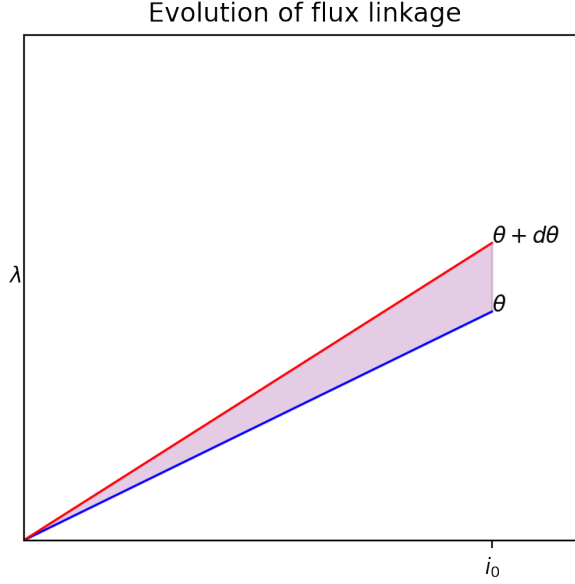


Figure 1.4. Evolution of the potential energy in a linear system as the movable element translates through an infinitesimal displacement $d\theta$. The change in potential energy of the system is shown as the shaded area between the curves.

For this linear system, the potential energy is easy to evaluate from eqs. 1.7, 1.1, and 1.2, as shown in eq. 1.9

$$W = \int_0^{\lambda_1} i \, d\lambda = \int_0^{\phi_1} i \, N d\phi = \int_0^{i_1} i N \mu \, di = \frac{\mu N}{2} i^2 = \frac{1}{2} L i^2 \quad (1.9)$$

If the current is kept constant while the plunger is inserted, the energy gradient depends only on μ , shown in eq. 1.10

$$F = \frac{dW}{dx} = \frac{N i^2}{2} \frac{d\mu}{dx} = \frac{1}{2} i^2 \frac{dL}{dx} \quad (1.10)$$

To put this into words, the force on the plunger is proportional to the derivative of inductance, or that the plunger experiences a force to bring it into that position with maximum proclivity to create magnetic flux.

Note that in all these cases, the flux ϕ and flux linkage λ are linearly proportional to current i . This is a reasonable approximation for air-wound coils at any current or for ferrous materials at small currents, but in magnetic circuits with ferrous materials at typical currents, the flux is sub-linearly related to current, as seen in Fig. 1.5. This may be explained by closer inspection of the behavior of magnetic circuits and magnetic flux.

As a convenient tool for analysis, magnetic flux ϕ and flux density \vec{B} are often compared directly to electric current i and electric current density \vec{J} , but the phenomena are fundamentally different. Amperian current is by definition the transport of an electric charge. Magnetic flux is defined as a surface integral of the magnetic B field: $\phi = \int \vec{B} \cdot d\vec{A}$. When an electric charge moves through a resistive medium, energy is dissipated, implying that a power is required to maintain an electric current. Magnetic circuits borrow many properties from electric circuits, namely reluctance. The electric property of resistance is so named because a resistive material will "resist" the motion of charge; the magnetic property of reluctance similarly "resists" the establishment of a magnetic field, but while power is required to maintain an electric current, power is only required to establish a magnetic flux, after which no power is required to sustain the magnetic flux.

The physical constant of magnetic permeability μ represents the propensity of a material to form a magnetic flux from a magnetomotive force. In ferrous materials, μ_{Fe} may be hundreds of times greater than μ_0 in a vacuum. The ferrous material has this strong propensity to form a magnetic flux because the electron orbits in a ferrous material tend to align themselves with an external magnetic field such that the field is amplified. At small values of H , this leads to very large values of B , but this amplification does have an upper limit.

After the electron orbits become completely aligned, the magnetic flux can be increased further by increasing i , although the incremental increase in B is proportional to μ_0 , which is significantly smaller than the initial incremental increase, μ_{Fe} . This can be described as

if the magnetic flux induced in a vacuum is always available without limit, and the flux induced in a ferrous material is added on top of this; the ferrous flux is just limited in its magnitude.

1.6 Nonlinear energy conversion

If a magnetic device is operated at small currents, it may be sufficient to analyze and describe the device with a linear model. In practice, most electric machines are operated with magnetic fields that enter well into the saturation region of the core in order to extract as much torque from the machine as possible. The effects of saturation are explored in this section, further using the solenoid as a tool of explanation.

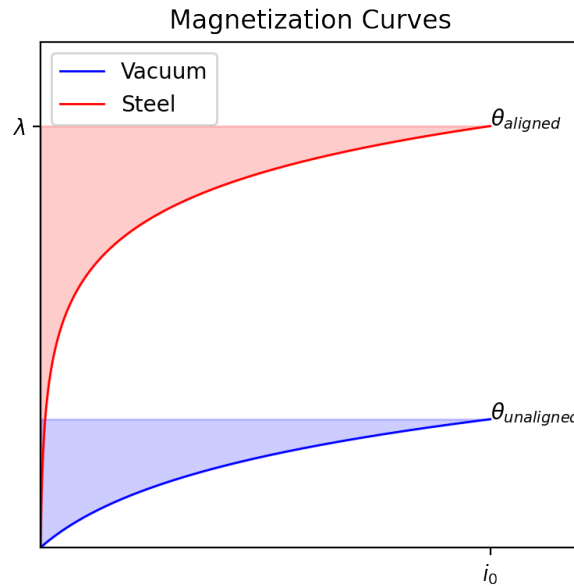


Figure 1.5. Magnetization curve for a system in a high permeability configuration (steel or aligned) and in a low permeability configuration (vacuum or unaligned).

In the solenoid, the \vec{H} field is directly and linearly proportional to the current, but the \vec{B} field and thus flux are sublinearly related. The \vec{B} field will increase very rapidly for small values of \vec{H} , but as \vec{H} grows larger and larger, the incremental change in \vec{B} becomes very

small. Because \vec{B} is directly proportional to ϕ and \vec{H} is directly proportional to i , the relation between ϕ and i has an analogous relationship. This sub-linear relationship is illustrated in Fig. 1.5. For small values of i , the slope of the line is proportional to μ_{steel} and for large values of i , the slope of the line is proportional to μ_0 .

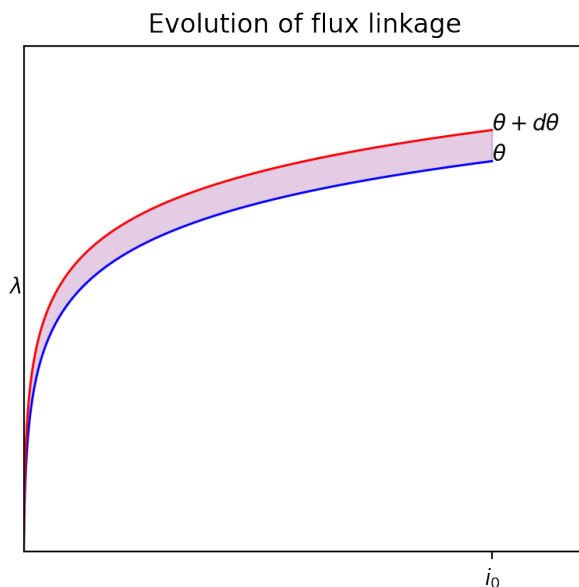


Figure 1.6. Differential change in potential energy as the system evolves from the empty (vacuum or unaligned) to full (steel or aligned) configurations.

The linear energy conversion principles from section 1.5 remain valid in the nonlinear case. The energy stored in the magnetic field is again represented by eq. 1.7, although for the saturated solenoid, no closed form exists to evaluate this potential energy. The potential energy integral is represented by the shaded areas of Fig. 1.5. When the plunger is removed from the solenoid, the flux linkage versus current follows the blue curve, and while the solenoid is inserted, the flux linkage versus current follows the red curve.

As the plunger is inserted into the solenoid, the flux linkage curve will evolve as shown in Fig. 1.6. Just as described in the linear version, Fig. 1.4, the infinitesimal work performed on the plunger as it traverses an infinitesimal displacement is shown in the shaded region.

The area swept out by the flux linkage curve in saturated conditions is greater than the area swept out in the linear case, which results in more torque.

From the analytic perspective of energy conversion in an electric machine, be it a solenoid and plunger or a SRM, the phenomenon of saturation does not affect the relation between force or torque production and energy; the same equation holds, although finding a closed form to describe the energy becomes more challenging. From a practical perspective, saturation places an upper bound on the force which can be produced.

1.7 Linear model of the SRM

Consider a traditional SRM with 6 stator poles and 4 rotor poles, illustrated in Fig. 1.7. The motor has 3 phases, and each phase is wound around two opposing stator poles. The polarity of the phase windings is such that the magnetomotive force is pointing inward from one stator pole, and outward on the opposing pole, so as to establish a flux as illustrated in Fig. 1.9.

If phase A is excited, eq. 1.5 can describe the torque experienced by the rotor, with the modification that the derivative is taken in rotational form, rather than linear. The rotor will tend towards the position so that two rotor poles are aligned with the stator poles of phase A. Equation 1.8 shows that the rotor experiences a torque to align itself in the position with maximum flux. From inspection, this must occur at the position shown in Fig. 1.7; this is referred to as the "aligned" position, and it is a stable equilibrium.

If an aligned position exists, then it follows that another position should be called the "unaligned". This is illustrated in Fig. 1.8. At this position, the magnetic flux is at a minimum and the torque is zero, but this is an unstable equilibrium. With a slight perturbation, the motor will experience a force which turns the rotor to the nearest stable equilibrium.

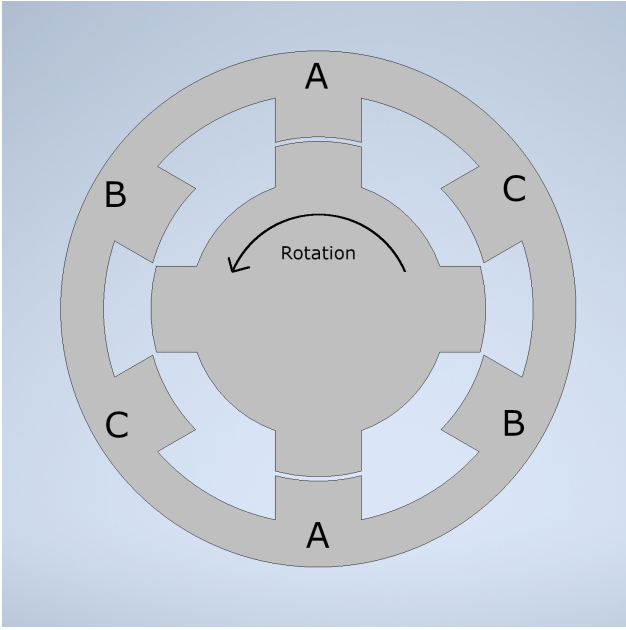


Figure 1.7. Physical model of a theoretical SRM, shown in the aligned position for phase A.

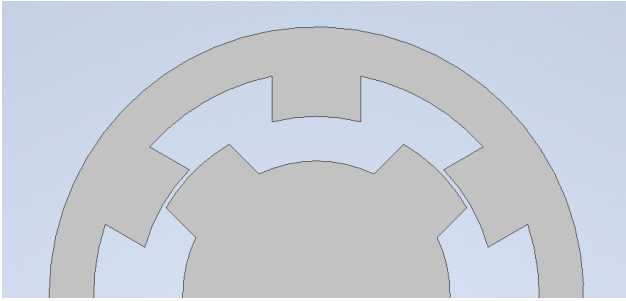


Figure 1.8. Switched reluctance motor shown in the unaligned position for phase A

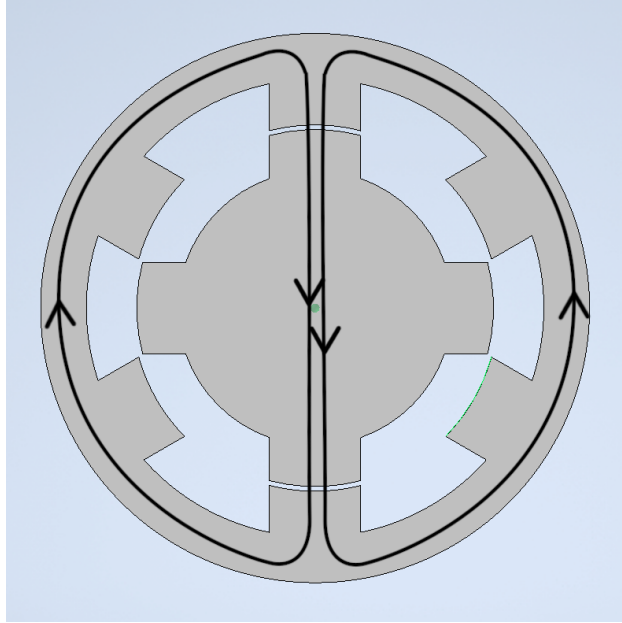


Figure 1.9. Flux path through the SRM in the aligned position, with phase A active.

Consider the flux path shown in Fig. 1.9. The flux path travels through the stator, one air gap, through the rotor, through another air gap, then finally through the back iron to where it began. For this linear model, the reluctance of steel is neglected ($\mu = \infty$), and the air gap is the only source of reluctance. The reluctance seen by the flux as it travels around the motor is given in eq. 1.13, which is twice the reluctance of a single airgap.

The equivalent magnetic circuit is shown in Fig. 1.10. The node on the right side represents the rotor, and the node on the left represents the stator. Because of the symmetry between R1 and R2, no flux will flow through any reluctance except for the phases which are excited. In single-phase excitation, this means that phases B and C can be neglected. Because of symmetry between R1-A and R2-A, and mmf1-A and mmf2-A, the flux in the circuit can be wholly described using the circuit in Fig. 1.11.

The total potential energy in the SRM is given in eq. 1.11.

$$W_{\text{total}} = i_a \lambda_a + i_b \lambda_b + i_c \lambda_c \quad (1.11)$$

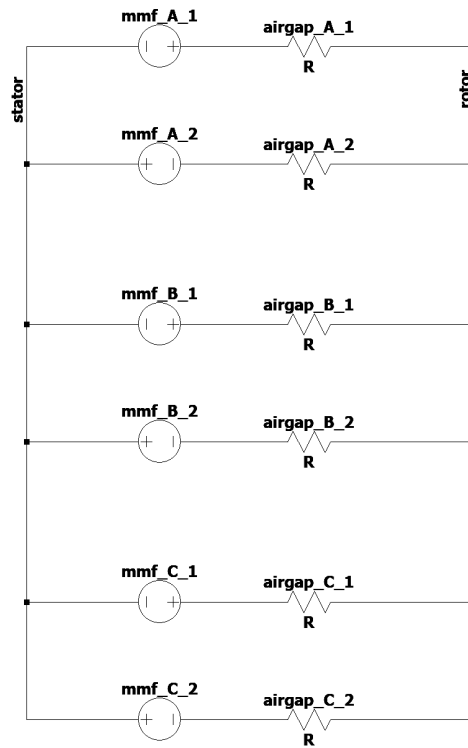


Figure 1.10. Equivalent magnetic circuit of the SRM showing all airgap reluctances and all phase windings

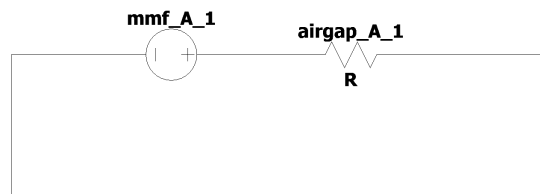


Figure 1.11. Simplified magnetic equivalent circuit used to describe the flux through the motor with single-phase excitation.

If the currents in phase B and C are zero, in the case of single phase excitation, the total potential energy reduces to that shown in eq. 1.12.

$$W = i_a \lambda_a \quad (1.12)$$

$$R_{\text{total}} = 2 R_{\text{airgap}} = \frac{2g}{\mu_0 A_{\text{pole}}} \quad (1.13)$$

The coils on phase A create a magnetomotive force f according to the number of turns N and current i , inducing a magnetic flux ϕ in the motor. The flux will flow according to eq. 1.14. Because there are two coils in series, the f is multiplied by 2.

$$\phi_{\text{phase}} = \frac{f_{\text{total}}}{R_{\text{total}}} = \frac{2Ni}{2\frac{g}{A\mu_0}} = \frac{ANi\mu_0}{g} \quad (1.14)$$

Rearranging eq. 1.14 in terms of flux linkage results in eq. 1.15.

$$\lambda_{\text{phase}} = N\phi = \frac{A_{\text{pole}}N^2i\mu_0}{g} \quad (1.15)$$

The torque can be described from eq. 1.5 in rotational form and 1.8 applied to eq. 1.15, resulting in eq. 1.16

$$T = \frac{\partial}{\partial \theta} \lambda_{\text{phase}} = \frac{N^2i\mu_0}{g} \frac{\partial}{\partial \theta} A \quad (1.16)$$

The only quantity which changes with angular position is the area of pole overlap in the motor. The area of a single pole is described in eq. 1.17, where l is the stack length and r is the mean airgap radius.

$$A = \begin{cases} lr\theta & \text{overlap increasing} \\ lr\Phi_{pw} & \text{poles overlapped} \\ lr(\Phi_{pw} - \theta) & \text{overlap decreasing} \\ 0 & \text{otherwise} \end{cases} \quad (1.17)$$

Substituting eq. 1.17 and 1.14 into the rotational form of eq. 1.5 yields the torque of this motor under single phase excitation in eq. 1.18.

$$T = \frac{l N^2 i \mu_0}{g} \cdot \begin{cases} 1 & \text{Overlap increasing} \\ 0 & \text{poles overlapped} \\ -1 & \text{Overlap decreasing} \\ 0 & \text{otherwise} \end{cases} \quad (1.18)$$

From eq. 1.18 the commutation pattern is clearly identified: apply current to a phase while the overlap and inductance are increasing, and extinguish the current before the overlap and inductance are decreasing. Because the motor has multiple phases, they can be activated in a sequential fashion to obtain continuous positive torque.

1.8 Other investigations

The concept of torque ripple reduction by means of a mechanical offset has been explored in other motors. Although the motor configuration and flux path are different for every example, the torque ripple was reduced in every case for a nonzero stator offset.

A double stator linear switched reluctance machine is investigated in the work by (Hirayama and Kawabata, 2017). The thrust ripple in this work mirrors the torque ripple found in the DSSRM in the single-phase mode of operation, discussed more in Chapter 4. By offsetting the two stators from one another by half of a pole pitch, the torque components contributed from each stator interfere destructively to reduce the torque ripple by about half.

An axial-flux switched reluctance motor is investigated by (Ma et al., 2014). The flux path in this axial motor passes from one stator, through the rotor segments, and into the other stator. The optimal offset between the two stators is actually quite small, with an offset of 0.375 degrees leading to a 18% reduction of torque ripple.

The segmented DSSRM in (Lee et al., 2017) uses a flux path that crosses between both stators, and the traditional concentrated tooth winding configuration. The flux path is the traditional long path. It is shown that a mechanical offset of about one third of the stator pole pitch yields a 35% reduction in torque ripple.

A multitoothed DSSRM is constructed in (Lee et al., 2014) with a rotor consisting of a unified body and salient poles protruding from the inner and outer surface of the rotor. In this work, rather than offset the stators, the rotor poles are shifted from the inner to the outer surface, leading to a reduction in torque ripple of 46% for a rotor pole offset of one third the pole pitch, just as in his related work (Lee et al., 2017).

CHAPTER 2

NUMERICAL ANALYSIS

The DSSRM is simulated using Ansys Maxwell, a finite element analysis (FEA) software package. FEA shows the magnetic fields inside the motor which cannot be directly measured in a physical prototype. The simulation environment also allows for idealized measurements that can theoretically be measured from a prototype, but are difficult to obtain in practice, such as the back emf.

2.1 Simulation

2.1.1 Physical setup

The motor consists of 3 major components: a rotor, an outer stator, and an inner stator, each created from magnetic steel. The rotor is created from six discrete bodies with a vacuum in between. The geometry of all steel bodies is taken directly from the prototype used in (Abbasian et al., 2010). The choice of this prototype is not arbitrary; the design of this motor underwent minimal optimization compared with subsequent prototypes. The prototype as developed in (Maharjan et al., 2018) has geometric contouring on the rotors, discussed more in (Wang et al., 2015), which leads to a torque ripple reduction by strategic localized saturation. The square-cut edges of the motor selected for this investigation do not use such a strategy to reduce torque ripple, and as such, this investigation can more directly assess the merits of a stator offset.

The motor uses solid copper regions for the windings. The motor contains separate windings for the inner and outer stator, just as in the real prototype. This allows measurement of the back emf and inductance values on the outer and inner stator separately. The windings and steel bodies can be seen in Fig. 2.1. The steel parts are configured to behave with the

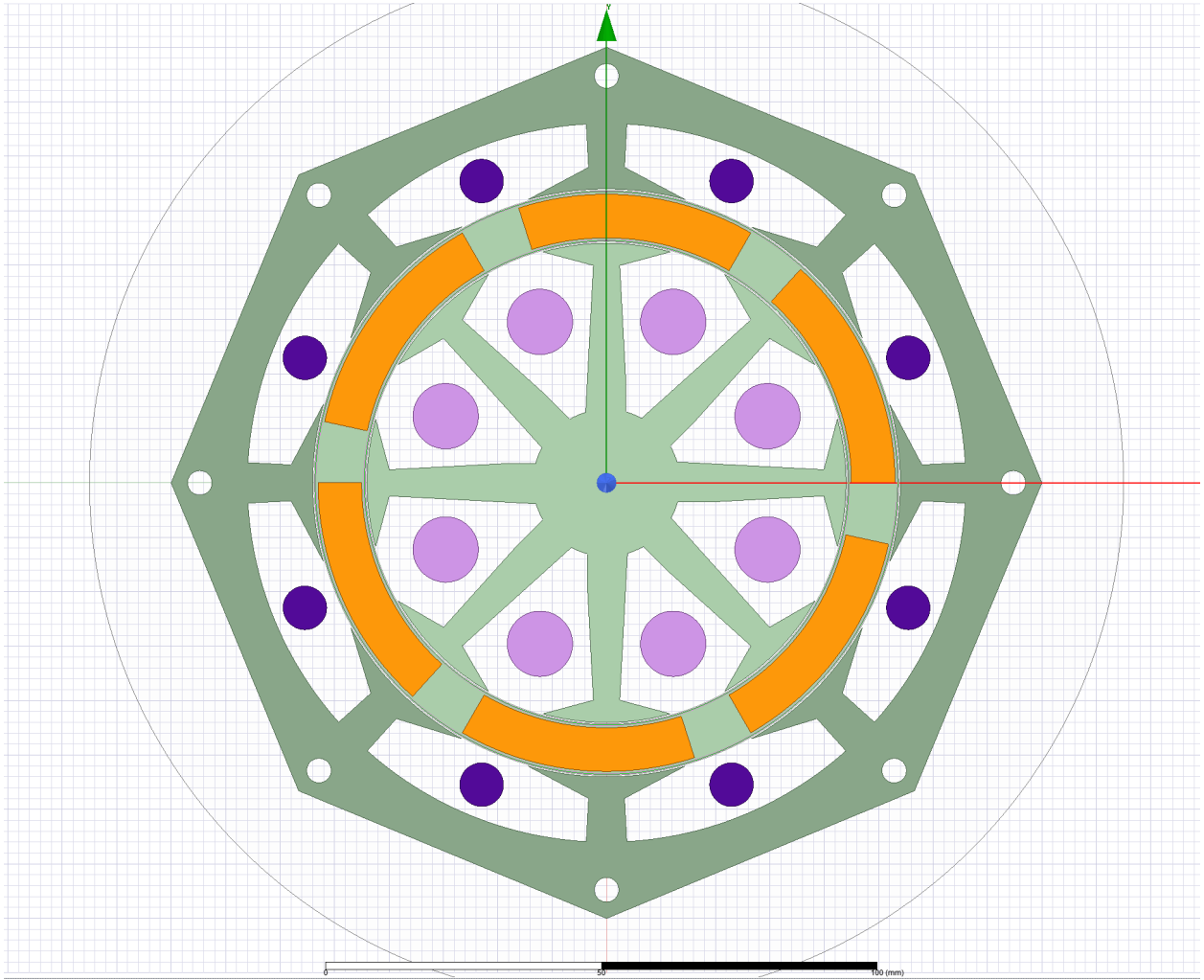


Figure 2.1. Physical model of the DSSRM

properties of M19 steel, laminated with a 95% stacking factor. The parameters of the motor are listed in Table 2.1 at the end of this chapter.

The real motor uses an aluminum rotor cage as the main structure to the rotor; at high speeds, this cage will result in significant eddy current losses. Neglecting to include the aluminum cage for simulation is acceptable for a quasi-static simulation such as this, because the losses will be negligible at low speed operation. The focus of of this investigation is the static torque profile, which will differ significantly from the torque profile observed at

high speed operation due to higher core losses and current transient effects, as well as the vibrational dynamics of a real motor. All these effects are out of scope of this investigation.

2.1.2 Electrical setup

The DSSRM contains 8 phases - four inside and four outside. The real prototype is wired with the inner and outer stator connected in series; to achieve the same motor behavior, the same current is applied to the inner and outer stator.

Stranding is not considered in the phase windings of the simulated motor. A solid region of copper is used, and the excitation is increased by $N = 50$ times, to reflecting the 50 turns per phase of the prototype. As an example, to simulate the behavior of the motor with a nominal 10A excitation, the windings in simulation will be excited with $50 \times 10\text{A} = 500\text{A}$.

2.1.3 Motion setup

The motion band is a ring that covers all of the rotor segments, illustrated in Fig. 2.2. All bodies within the motion band move together about the Z-axis with constant angular velocity. A clockwise rotation is positive.

To obtain the static torque profiles, a very low angular velocity is used: 10 rpm. This is low enough that core losses are negligible and the torque differs only an infinitesimal amount from the true static torque profile.

2.1.4 Transient setup

A transient simulation is used to obtain the motor data. The simulation will run from $\theta_0 = 0$ at $t = T_0 = 0\text{s}$ to $\theta_1 = \Phi_{\text{rpp}} - \Delta\theta_{\text{step}}$ at $t = T_1$, with Φ_{rpp} being the pole pitch of the rotor. The zero position is illustrated in Fig. 2.1. The time step is calculated to achieve an angular displacement $\Delta\theta_{\text{step}}$ of 0.5° per step. The total number of steps is given by

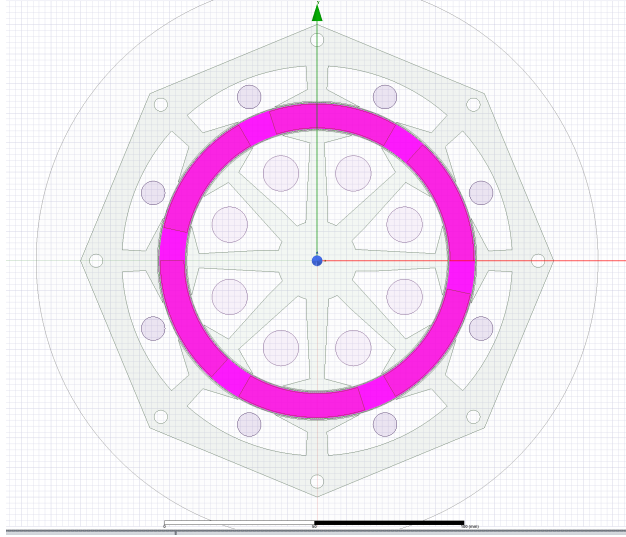


Figure 2.2. Motion band for the DSSRM. All objects inside the highlighted ring move at constant angular velocity.

$$n = \frac{\Phi_{\text{rpm}}}{\Delta\theta_{\text{step}}} = \frac{60^\circ}{0.5^\circ} = 120 \text{ steps} \quad (2.1)$$

The end time T_1 is calculated by

$$T_1 = \frac{\Phi_{\text{rpp}} - \Delta\theta_{\text{step}}}{\omega_{\text{rpm}} * 60} \quad (2.2)$$

2.1.5 Input parameters

The main parameter adjusted in this simulation is the stator offset angle. The simulation is repeated from complete misalignment in one direction to complete misalignment in the other. With the stator pole width of 45° , the extreme values of $[-22^\circ, 22^\circ]$ are selected, with a step size of 1° .

The other parameters pertain to the current injected to the motor. The simulation is repeated for phase currents of 10A for unsaturated conditions and 30A for saturated conditions. Because this motor can be operated with single-phase excitation and two-phase

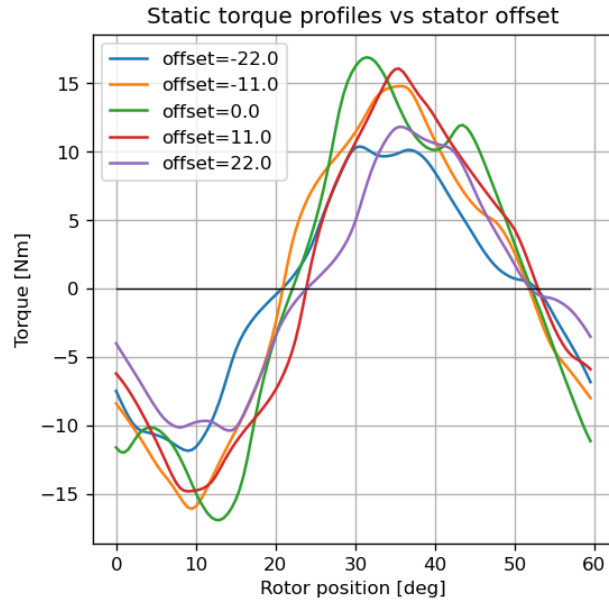


Figure 2.3. Static torque profiles from the motor with some arbitrary stator offsets.

excitation, the simulation is repeated for each scenario: only phase A is active for single phase excitation, and phase A + B active for two-phase excitation.

2.1.6 Output data

The most important output data is the torque profile from the motor. This can be conceived as a scalar torque value in a high-dimensional grid with coordinates of time, stator offset, current vector permutations, and current magnitude. The motor is operated with all parameters fixed except for time, which yields a continuous torque profile as a function of time, or equivalently, as a function of rotor position. A selection of static torque profiles can be seen in Fig. 2.3.

While the torque is the main information extracted from simulation, the inductance matrix and back-emf are exported as well. These are all scalar values that depend on time and the other parameters, just like the torque data.

While the input current requires preprocessing, the flux linkage and inductance must be similarly postprocessed. The phase inductance must be multiplied with $N^2 = 2500$, and the flux linkage must be multiplied with N to realize the values realized in the physical motor.

2.2 Data analysis

The motor in simulation has a constant DC current at all times; this is useful to obtain the static torque profile, but the motor under operation will use commutated phase currents. The metrics used to assess the behavior of this motor are the mean torque and torque ripple, which are only meaningful in the context of a motor with a nonzero mean torque. In other words, to assess the performance of the motor from simulation, the torque profile from commutated currents must be extracted somehow from the static torque profile. This commutated torque profile will be found using two basic assumptions.

First, a phase shift in phase currents will yield an identical phase shift in the static torque profile. In other words, if the motor is excited with a current of 30A in phase A, the torque from a motor excited in phase B will be identical to that from phase A with a phase shift of 45° corresponding to the spatial separation between stator poles. This symmetry also applies to two-phase excitation, with the torque profile of phase A and B being shifted 45 degrees from the torque profile of the motor with phases B and C active.

Second, for a given rotor position, phase excitation, and stator offset, the motor will output a torque as specified by point on a static torque profile obtained by simulating the motor under those conditions. This means that if we excite the motor for some time interval using phases A and B, the torque profile will exactly match the static torque profile for that excitation pattern; if we then deactivate phase A and activate phase C, the commutated torque profile will be identical to the static torque profile from activating phase B and phase C, as obtained from the first assumption. This commutation strategy can be seen in Fig. 2.4.

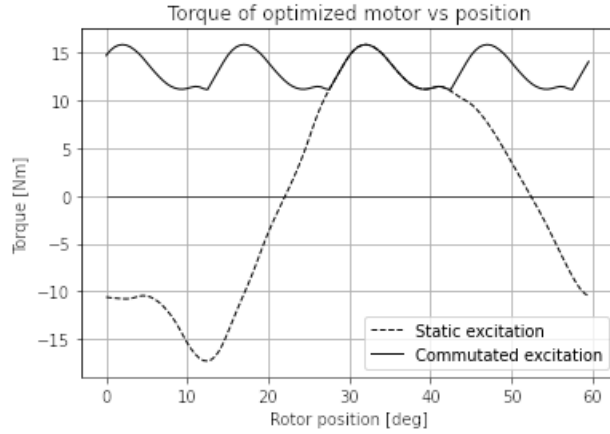


Figure 2.4. Commutated torque profile and the corresponding static torque profile used to derive it.

2.2.1 Objective function

The optimization of this motor is performed with simulated data. To facilitate a meaningful definition of a "better" or "optimal" torque profile, some metrics must be established. The mean torque and torque ripple have been mentioned previously; let them be defined rigorously below as \bar{T} and R .

$$\bar{T} = T_{\text{mean}} \quad (2.3)$$

$$R = \frac{\Delta T}{\bar{T}} = \frac{T_{\text{max}} - T_{\text{min}}}{\bar{T}} \quad (2.4)$$

For the static torque profile, the mean torque will be zero and the torque ripple will be undefined as a result. These metrics are only meaningful when applied to the commutated torque profile as described above.

In order to simplify the optimization, an objective function $O(T)$ is defined in eq. 2.5 which is optimal for a maximum value. The value for R will be in the neighborhood of $[0.1, 1]$ while the value for T will be in the neighborhood of $[10, 15]$, which indicates that R has a

much stronger influence on the objective function. This is the intended effect because while mean torque must not be penalized excessively, the torque ripple is the primary metric to improve. Note that all units in this equation are neglected.

$$O = \frac{\bar{T}}{R} = \frac{\bar{T}^2}{\Delta T} \quad (2.5)$$

As described above, the torque profile is positive because the current is commutated at the right moment. This is called the firing angle, and its selection is important for the optimal behavior of the motor. For each stator offset, the torque profile is obtained by repeating a segment of the static torque profile starting at the firing angle and ending at the extinction angle. The extinction angle is the firing angle plus the dwell angle. The dwell used in this work is given as ϕ_{dwell} from eq. 2.6 with N_{active} representing the number of phases active at a given time. If the motor is operated with two phases active at a time, this corresponds to a dwell of $30^\circ_{\text{mech}} = 180^\circ_{\text{elec}}$, and if the motor is operated with a single phase active at a time, this corresponds to a dwell of $15^\circ_{\text{mech}} = 90^\circ_{\text{elec}}$. In either case, the length of the torque segment used to construct the running torque profile is $15^\circ_{\text{mech}} = 90^\circ_{\text{elec}}$.

At stator offsets other than nominal, the optimal dwell of the motor may change, due to an asymmetric static torque profile. This effect is neglected and dwell is not considered in the optimization.

$$\phi_{\text{dwell}} = \frac{\phi_{\text{rpp}}}{N_{\text{phases}}} N_{\text{active}} \quad (2.6)$$

The firing angle has a large effect on the performance metrics. The mean torque may drop and the torque ripple will increase significantly for the wrong firing angle, illustrated in Fig. 2.5. For this reason, the firing angle at each stator offset is chosen to maximize the objective function. Practically, this means that the commutation usually occurs at the moment that the torque profiles overlap between subsequent phases, but this may not always be the case.

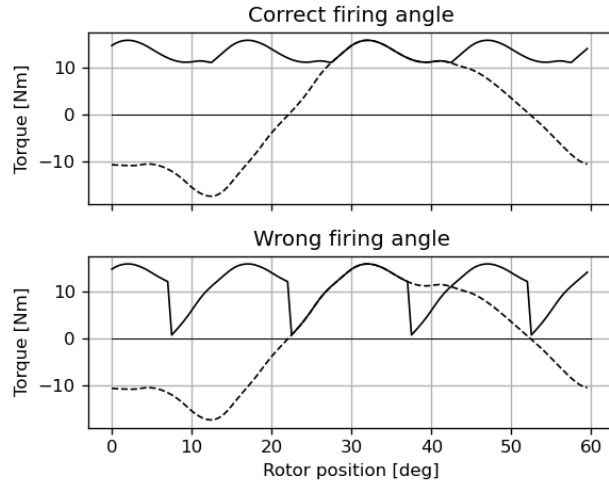


Figure 2.5. Commutated torque profile with the correct firing angle and an arbitrarily selected incorrect firing angle.

Because the commutated torque profile is a repeated segment taken from the static torque profile, the mean and torque ripple of the entire commutated profile can be described by analyzing only the segment. The maximum, minimum, and mean of the entire torque profile are the same as those values from the torque segment.

Once the torque ripple, mean, and torque are known for each firing angle, the highest objective is collected and these metrics become the values used to describe that stator offset. The best values for each stator offset can then be compared. The optimal stator offset is that which produces the highest objective. The optimization is repeated separately for the case of single-phase excitation and two-phase excitation. The performance metrics are plotted in Fig. 2.8 and 2.6 for each stator offset.

2.3 Optimization results

The optimization results of the motor are different depending if the motor is operated in single-phase or two-phase mode.

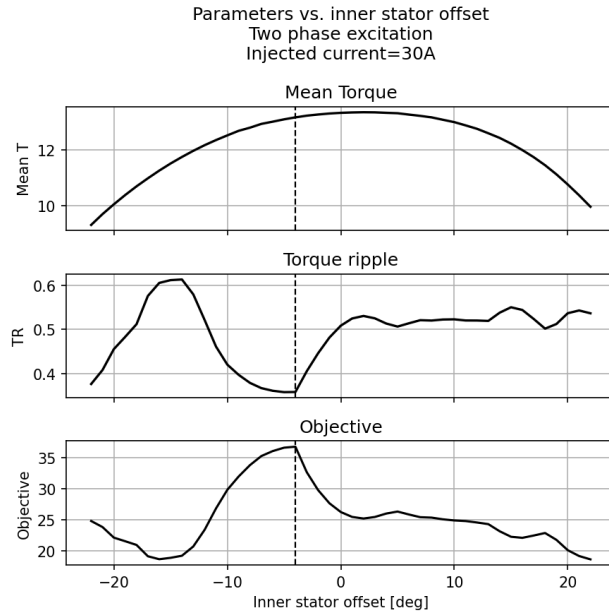


Figure 2.6. Performance metrics vs stator offset for two-phase operation of the motor.

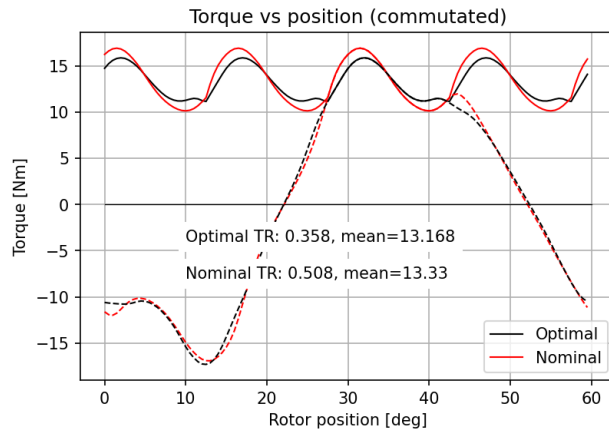


Figure 2.7. Nominal vs optimal torque profiles of the motor operated in two-phase mode. The red line represents the commutated and static torque profile of the original motor, while the black line represents the commutated and static torque profile of the optimized motor.

For two-phase excitation, the optimal stator offset is $\phi = -4^\circ$. This leads to a reduction in torque ripple of 36% and a mean torque reduction of about 1%. The two-phase torque profile can be seen in Fig. 2.7.

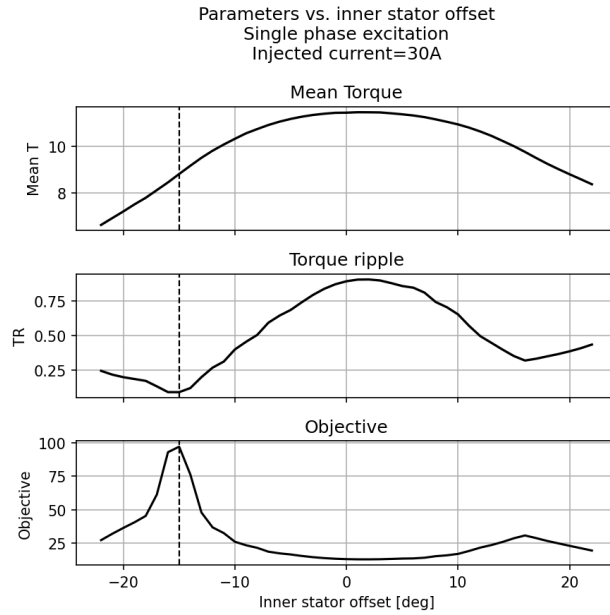


Figure 2.8. Performance metrics vs stator offset for single-phase operation of the motor.

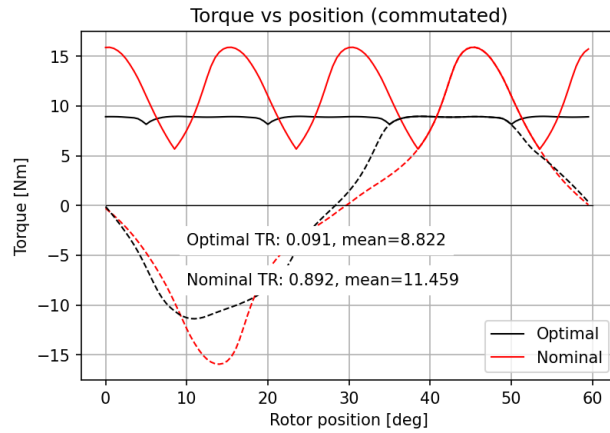


Figure 2.9. Nominal vs optimal torque profiles of the motor operated in single-phase mode. The red line represents the commutated and static torque profile of the original motor, while the black line represents the commutated and static torque profile of the optimized motor.

For single-phase excitation, the optimal stator offset is $\phi = -15^\circ$. This leads to a significant reduction in torque ripple of 90%, but a larger mean torque penalty of 20%. The single-phase torque profile can be seen in Fig. 2.9.

Table 2.1. Machine Parameters

| Parameter | Value |
|----------------------------------|---------------|
| Number of stator poles | 8 |
| Number of rotor poles (segments) | 6 |
| Number of phases | 4 |
| Outer radius of inner stator | 44mm |
| Inner radius of outer stator | 54mm |
| Thickness of rotor segment | 8mm |
| Stack length | 115mm |
| Airgap (each side) | 1mm |
| Arc of rotor segments | 47.75° |
| Number of turns per phase | 50 |
| Rated current | 30A |
| Rated voltage | 100V |
| Resistance of inside phase | 0.25 Ω |
| Resistance of outside phase | 0.50 Ω |
| Wire material | Copper |
| Core material | M19 steel |
| Mass of copper | 3.1kg |
| Mass of core | 5.0kg |

CHAPTER 3

EXPERIMENTAL VALIDATION

The purpose of experimental validation is to verify the results from simulation. The performance of the motor will be observed at two points: nominal and optimal, for the two-phase mode of operation. The single-phase mode of operation will not be explored experimentally.

The torque of the motor is recorded in normal operation for measuring the average torque and torque ripple, and the torque of the motor is measured under static excitation to obtain the static torque profile.

This chapter will be arranged as follows. First, the experimental setup and major components are described. Next, the inverter firmware and control diagram are explored. Following the inverter software, the methods used for recording and processing the data are discussed. Finally, the experimental results will be presented.

3.1 Test platform hardware

The test platform may be seen in Fig. 3.1. The major components in the test platform are:

1. DSSRM
2. Inverter
3. Mechanical load
4. Torque meter
5. Encoder
6. Power supply

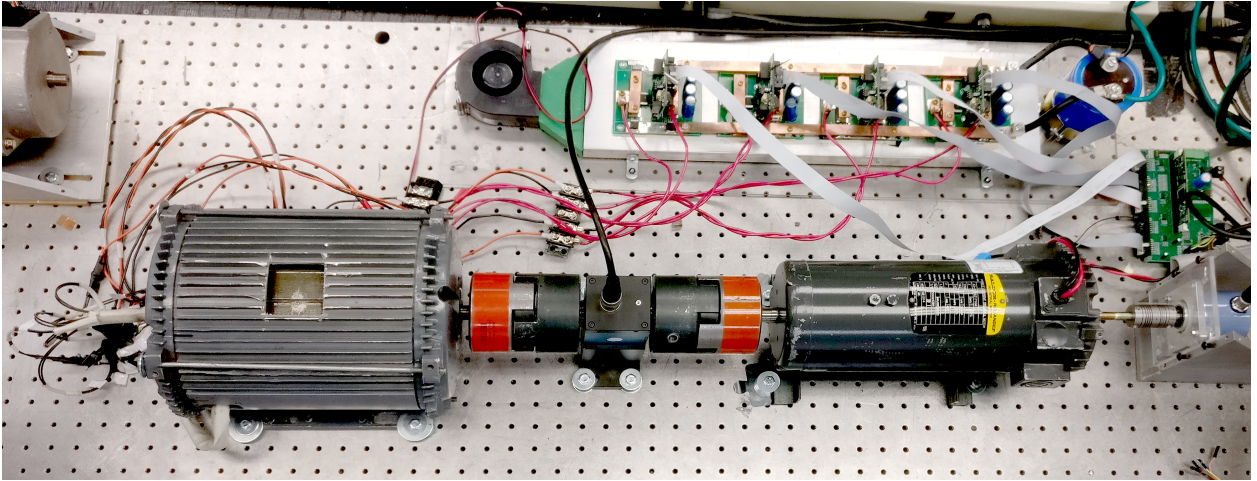


Figure 3.1. Test platform used for evaluating the DSSRM. Not shown are the high voltage power supply and electronic load. This illustration ©2019 IEEE (Hair et al., 2019)

The DSSRM is the same prototype as constructed and measured by (Abbasian et al., 2010) among other works. The motor is wound in such a way to give access to the inner and outer stators separately, and they are connected in series.

This particular motor was selected above others because it was the first prototype in this family of motors, and does not contain significant optimization. Notably, the rotor segments have a square edge as shown in Fig. 2.1. Subsequent motor prototypes have optimized rotor shapes such that the center of the rotor faces are cut away, leaving a hollow "V" shape that results in lower torque ripple. Using this motor with square-cut rotor segments allows for a more direct assessment of the merits of stator offset. One further benefit of this prototype is that the inner and outer stator may be rotated arbitrarily with reference to each other thanks to the specific motor frame used.

The inverter consists of four fully-independent H-bridge modules. This provides more sophistication than is required for operating the DSSRM, namely the capability of bidirectional phase currents. At the beginning of this investigation, bidirectional currents were considered, but the simpler unipolar excitations were sufficient to create the desired flux path. The full

H-bridge inverter has an increased cost in the form of two additional MOSFETs per phase as well as their associated driving circuitry, but this increased cost is irrelevant in the academic setting, especially considering that this inverter was repurposed from a past project. The inverter has current feedback for each phase, but does not have voltage feedback for the phases or the DC bus; these measurements are sufficient for operating the motor with hysteresis current control. The inverter also contains an encoder interface.

The mechanical load shown in Fig. 3.1 is a permanent magnet brushed DC motor, although this motor was not used as the main mechanical load in this work. The motor and the e-load used to control the motor were incapable of operating at very low speed and thus were not useful for measuring the static torque profile of the motor. Instead, two alternative methods were employed to load the motor. For measuring the torque profile of the motor in normal, commutated operation, a rope brake was used. For measuring the static torque profile, a manual crank was used. These methods will be discussed in more detail in section 3.3.2 and 3.3.1.

The torque meter is a Kistler 4502A in the range of $\pm 100\text{Nm}$, with a cutoff frequency of 2kHz. The torque meter outputs an analog signal in the range of $\pm 5\text{V}$, with zero voltage representing zero torque. The signal from this torque meter is further treated with a first order low pass filter at 500Hz; this will limit the measurement of torque ripple at high speeds, but the inertia of the rotating system along with the compliant coupling create an intrinsic mechanical low pass filter, so the torque experienced by the torque meter at high speed would not represent the static torque profile anyway.

The position feedback is provided by a 12-bit incremental encoder. It outputs two square waves offset by 90° as well as a third channel which produces one pulse per revolution. In one revolution, each square wave will produce 2^{12} edges, for a total of 8192 edges per revolution. Due to the 90° offset between the A and B outputs, every level change on either channel can be interpreted as a single step forwards or backwards by $\frac{1}{8192}$ revolutions. The single pulse

on the index channel provides a mechanism to reset the position to an absolute reference to correct for any missed steps.

The high voltage power supply is capable of providing 100V and 100A. It is connected to an enable signal which is brought low by depressing the emergency stop button. The emergency stop button does not control any devices other than the high voltage power supply.

3.2 Inverter software

The inverter software performs several tasks, the most noteworthy of which being:

1. Periodic task management
2. Current measurement
3. Fault condition monitoring
4. Current control
5. Position and speed monitoring
6. Speed control
7. Current commutation
8. Analog feedback

3.2.1 Periodic task management

The inverter runs a main interrupt routine with a periodic trigger. A PWM module is used to generate an interrupt at 50kHz which triggers the analog to digital converter (ADC) which itself generates a software interrupt, serviced by the main interrupt service routine

(ISR). The most critical tasks are completed at the full ISR rate: current monitoring, current control, and fault monitoring. The remaining tasks are called in slower periodic functions, at 1kHz. A rate multiplexer is used in favor of nested interrupts for the sake of simplicity.

3.2.2 Current sensing

The current sensing is achieved using the ADC. Each phase current is measured using an Allegro hall effect current sensor, and the signal is scaled and filtered on its way to the ADC. The ADC start of conversion (SOC) is triggered in hardware by a PWM module running at 50kHz. The analog to digital converter will convert all analog signals in one sequence, after which the ADC measurement result can be accessed in software. The sensing subroutine reads the ADC results, converts the result to a raw voltage present at the ADC pin, subtracts the bias offset voltage, and then multiplies by the current scaling. This task is run at full ISR speed.

3.2.3 Current control

The inverter controls the phase current by means of a hysteresis controller on each of four H-bridge modules. The controller defines an upper and lower limit on the current around a target current, called the hysteresis band. The upper and lower limit of the hysteresis band are separated from the reference current by a fixed interval. The current controller receives two pieces of information for each band: a boolean phase activation and a float phase reference current.

If the phase is active, the inverter will always apply a positive or negative voltage; if the phase is inactive, the inverter deactivates all switches on that phase, and the phase will see the full DC voltage in opposition to the phase current until the freewheel current drops to zero.

While a phase is active, the current controller monitors the current in the phase and if the measured current is above the hysteresis band, the inverter applies negative voltage, and if the measured current is below the band, the inverter applies a positive voltage. While the measured phase current is inside the acceptable band, the H-bridge state is not changed; if it is applying positive voltage, it will continue to apply positive voltage.

It is noteworthy that the switching frequency is not fixed; the current controller does not use PWM; the inverter is not guaranteed to change any switch states at an arbitrary interrupt. The control of switches in the H-bridge is achieved by software writes to the GPIO registers; this leads to poor fault tolerance in the case of a software glitch, as the switches will stay in the same state indefinitely if the CPU does not change their state, which could result in catastrophic damage from uncontrolled high currents. This poor fault tolerance could be improved significantly by a few methods.

First, the current could be controlled using an analog comparator subsystem such as the one available on the TI TMS320f28379; this would allow the current to remain in the fixed band even if the CPU halted, although the current reference would remain constant in such a case. Using a comparator would also remove the intrinsic ceiling on the switching frequency: with software switching, one switching cycle is guaranteed to require at least two interrupt cycles, leading to a maximum switching frequency of 50kHz.

Another method to improve robustness of the system would be to use two PWM outputs per phase, either on the top or bottom two switches, and set the PWM to a slower switching frequency with an action qualifier set to turn off the switches if the timer is not reset; the ISR could reset this timer at every switching cycle such that the PWM will never directly turn off the phase switches unless the ISR fails to service the PWM timer. This would be achieve similar functionality to a watchdog timer.

3.2.4 Position and speed monitoring

The position is monitored using the eQEP module on the microcontroller. The eQEP module contains a hardware counter that continuously monitors the edges from the encoder outputs A and B. When the first index pulse occurs, the position is saved, the hardware position counter automatically resets to zero, and henceforth the saved position of the first index is added to the position counter. This routine allows for finding and handling the first index event without requiring an explicit search for the encoder index.

The mechanical position in per-unit form is calculated by dividing the position counter by the total number of edges per revolution. The electrical position is calculated by multiplying the mechanical position with the number of rotor poles, then wrapping the value to the range $[0, 1)$. The speed is calculated by taking the quotient of the position change and the ISR period. The angular acceleration is calculated by taking a similar discrete derivative from the speed itself. Both the speed and angular position are filtered heavily before they are consumed by another part of the program. Control stability issues are not a concern because the torque of the motor is measured at low speed with the speed loop saturated, resulting in an open feedback loop.

3.2.5 Fault detection

The fault status of the inverter is monitored by checking every phase current and the speed for excursion beyond their acceptable ranges. If a fault event occurs, the state machine enters the "fault" state and the current controller shuts off all switches.

3.2.6 Speed control

The speed is controlled with a simple feedback loop with a PI controller. The inputs to the speed loop are a target speed and the actual speed, and the output is a single, scalar torque

request. It is easiest to consider this torque request as a reference current passed to the current commutator.

3.2.7 Current commutation

The current reference from the speed loop is passed directly to each phase current controller whenever the phase is active; this commutation action may be described similar to a distributor.

Each phase has a spatial offset from the first phase; phase B is offset by 45° , phase C is offset by 90° , and phase D is offset by 135° . For each phase, the electrical position is offset by the spatial phase offset and then is wrapped to within 360° . If the resulting value is greater than the firing angle and less than the extinction angle, the phase is active. The phase current will have a polarity selected to maintain the flux path shown in Fig. 1.1.

During the initialization phase at inverter boot, one phase current is excited until the motor settles into a stable equilibrium. This position is then saved as the zero position for phase A. This is critical for proper operation of the motor because the inductance is not monitored online, and current commutation is performed according to rotor position, not phase inductance.

3.2.8 Control block diagram

The components of the control diagram are described above. The diagram is shown in complete form in Fig. 3.2.

3.2.9 Analog feedback

The inverter must provide an analog signal to indicate the rotor position, although the TMS320f28335 does not have a digital-to-analog converter. A workaround is implemented by using a high-resolution PWM signal at 600kHz with a hardware RC filter at 15kHz. The

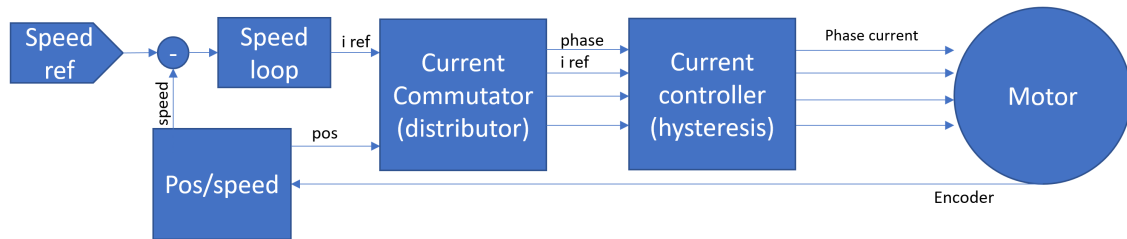


Figure 3.2. Control block diagram used to operate the DSSRM.

duty cycle of the PWM signal can be adjusted from 0-100%, providing an analog signal of 0-5v. The maximum voltage from the PWM will contain a gain error because the 5v comes from the bias supply on the inverter control board, rather than a precision reference. This is not a major concern because the analog feedback is used for a position signal, and as long as the voltage is somewhat stable within a mechanical cycle, the signal will provide sufficient fidelity. The minimum and maximum values of the analog signal are expected to be 0v and 5v, but in practice these values may differ from ideal; this is corrected while the data is postprocessed by converting the signal to per-unit magnitude, removing any zero offset and scaling the signal so that the maximum is 1 unit.

3.3 Experimental measurements

Two types of torque profiles are collected: static and commutated, and each requires its own type of mechanical load.

3.3.1 Static torque profile

To record the static torque profile, the motor is excited with a constant DC current and the current is not commutated. This results in a motor that will produce a mean torque of zero. It will rotate until it reaches a stable equilibrium, then remain in that position. To observe the static torque profile, the rotor must be turned using an external prime mover. The DC

motor could be used to turn the DSSRM, but the oscillatory torque profile would result in a varying speed, and the inertia of the rotating system would create a reaction torque that pollutes the true static torque profile.

To avoid the issues of nonuniform speed, a crank arm is attached to the motor shaft on the far side of the torque meter. The motor is then advanced manually through at least one electrical cycle, at very low speed and with very small angular acceleration to avoid the aforementioned issue of reaction torque. The torque and position are recorded using an oscilloscope. After recording this data, it is processed offline and plotted with the torque on the Y-axis and the position on the X-axis.

When rotating the motor in the positive direction, the friction will create a negative torque, and while rotating the motor in the negative direction, the friction will create a positive torque. The effects of friction can be corrected by rotating the motor in both directions, then taking the average torque at each position. This average is taken as the mean of all torque data points from a small interval around the position to be calculated.

3.3.2 Commutated torque profile

The commutated torque profile is easier to measure because the motor creates a positive mean torque and will rotate under its own power. As discussed previously, the DC motor is not used for loading the motor even in this case, as it cannot be operated at a low enough speed using the e-load available. As a simple workaround, a mechanical load is improvised. A strap is wrapped around the smooth surface of the coupling on the far side of the torque meter. One end of the strap is affixed to the table, while the other end is left free. When the free end is tensioned lightly, a large braking force is applied to the coupler. This is a band brake system, commonly called a rope brake dynamometer.

The torque and position information is recorded as above, using the analog feedback for position and the torque meter for torque information. An oscilloscope is used to record these

channels and, just as in the case of the static torque profile, the torque information is plotted versus the position.

3.3.3 Inductance profiles

The self inductance of the phase windings is measured for comparison with the simulated inductance profile. The inductance is measured for the series combination of phase A-inner and A-outer.

To measure the combined phase inductance, a current is applied to one phase with hysteresis limits at 0 and 10A, resulting in a triangle wave with frequency that changes according to phase inductance. A low DC bus voltage is used to ensure a reasonably low hysteresis frequency. The rotor is advanced manually while the phase current and rotor position are recorded. The inductance vs. position is calculated offline according to eq. 3.1, with T representing the period of the current waveform. This inductance profile is shown in Fig. 3.5.

$$L = \frac{TV_{dc}}{2i_{pk}} \quad (3.1)$$

3.4 Experimental results

The static torque profile for the nominal and optimal motor are shown in Fig. 3.3 along with the simulated torque profile for comparison. The torque profile is much smoother in the positive region compared with the unoptimized torque profile. Note that in this plot, the optimal offset is labeled at $\phi = -5^\circ$ while the result from Chapter 2 shows an optimal offset of $\phi = -4^\circ$. This is because the simulation was repeated twice for high-resolution and low-resolution time steps, and the results differ slightly with the higher resolution data; the difference of 1° is well within the margin of error for locating the proper offset in the motor, and for this reason the results of 4 and 5 degrees will be treated as the same result.

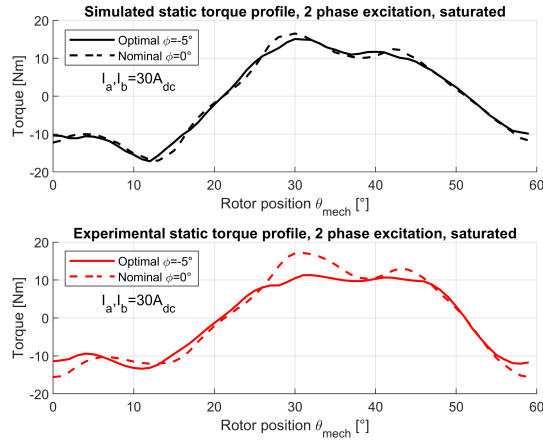


Figure 3.3. Static torque profile of the motor under two-phase excitation. The red dashed line is the torque from the nominal motor, and the solid red line is the torque from the optimized motor. This illustration ©2019 IEEE (Hair et al., 2019)

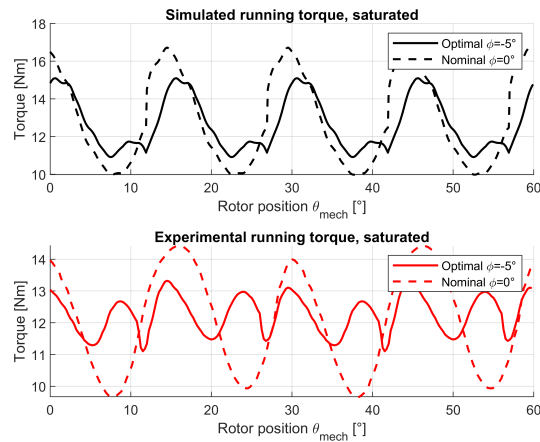


Figure 3.4. Commutated torque profile of the motor under two-phase excitation. The red dashed line is the torque from the nominal motor, and the solid red line is the torque from the optimized motor. This illustration ©2019 IEEE (Hair et al., 2019)

The commutated torque is shown in Fig. 3.4. While the simulation predicts a reduction of torque ripple by 36%, the experimental torque ripple reduction was 54%, a significantly better result. The mean torque was also predicted to decrease by about 1%, but the experimental mean torque increased by that amount rather than decreasing.

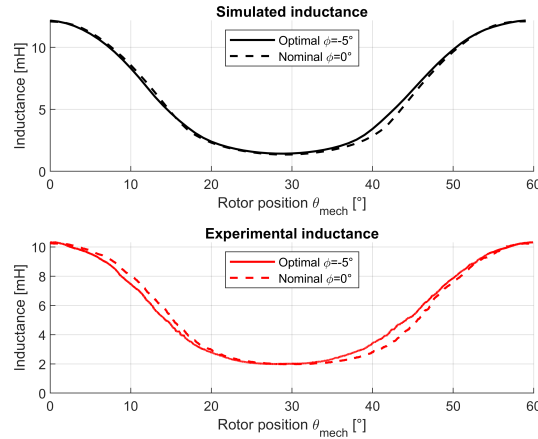


Figure 3.5. Inductance of phase A in the DSSRM for nominal and offset conditions. The top pane shows the predicted inductance from simulation, while the lower pane shows inductance measured experimentally as described in section 3.3.3. This illustration ©2019 IEEE (Hair et al., 2019)

To explain the discrepancy of the torque ripple, two possible explanations are presented. First, the simulation will likely have some errors and inaccuracies that restrict it from representing the true torque of the machine. Fringing fluxes in the Z -axis are one such example. The second explanation is that the motor is connected to the torque meter and encoder by means of a compliant coupling, which can easily compress by a few mechanical degrees under large torque. This would have the effect of rounding out the torque profile as measured experimentally.

The inductance profile of the motor in nominal and optimal configurations is shown in Fig. 3.5. The inductance profile evolves from nominal to optimal with a few features, most notably the longer but more gradual slope of the inductance in the optimized machine in comparison with the original configuration. Both the simulation and experiment show the same evolution.

CHAPTER 4

MECHANISM FOR TORQUE PROFILE IMPROVEMENT

This thesis has so far discussed the behavior of the motor in simulation and a verification of these results in the experimental setup, but a mechanism has not yet been presented for how the torque changes. The fundamental key used to describe how the torque profile changes is to consider the shaft torque as the sum of several different sources of torque. In this chapter, three mechanisms will be presented, in increasing levels of complexity.

First, the torque profile will be described using a harmonic analysis of the torque profile itself.

Second, the torque will be described from the perspective of electric power in each phase. The back emf and phase current will be used to estimate the component of torque generated in each phase winding and each stator separately.

Third, the torque will be described from the perspective of the inductance matrix. The inductance matrix describes not only the torque from each winding separately, but from the interaction between every active winding.

4.1 Harmonic analysis of torque profile

The torque profile of the running motor contains two peaks per commutation cycle, as seen in Fig. 2.4. The nominal motor has a large harmonic component at the commutation frequency, 4 times per electrical cycle. The optimized motor has a very small harmonic component at that commutation frequency, but has a large harmonic component at twice the commutation frequency. This can be interpreted as two stators each contributing to the shaft torque, and each stator's torque contribution having a peak.

If the torque contribution from each stator is in alignment, as in the lower plot of Fig. 4.1, the shaft torque will have a large harmonic component at the same frequency as the separate torque contributions.

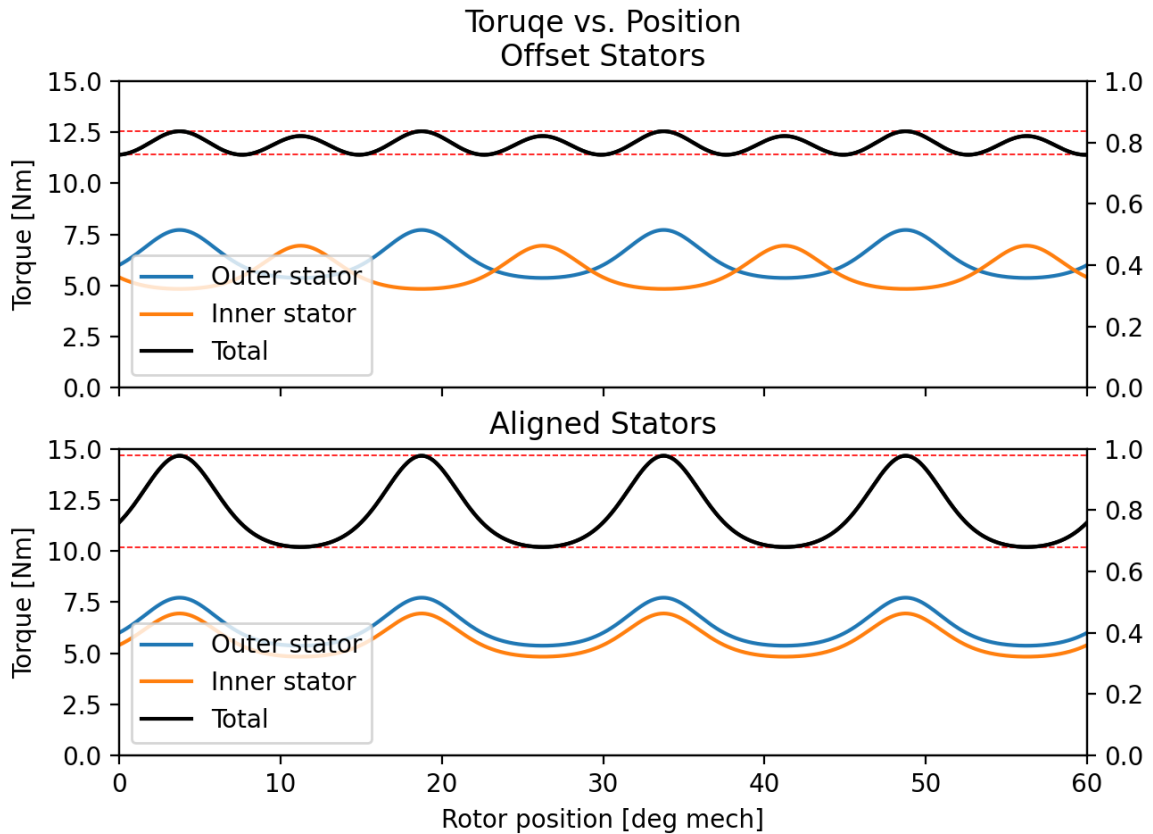


Figure 4.1. Model for interpreting harmonic content of torque profile. Each stator provides a torque contribution, and the sum is observed at the shaft.

If the torque contribution of each stator is misaligned, as in the upper plot of Fig. 4.1, the shaft torque will have a smaller harmonic component at the commutation frequency. The shaft torque will have a harmonic component at twice the frequency of the separate torque components. This is a desirable outcome because the variance of the torque waveform is reduced, but also the higher harmonic components will likely present less interference with normal operation of a motor drive system.

According to this perspective, the torque from each stator is created independently, and each stator will create a single peak of torque in each commutation cycle. This illustration

implies that a spatial phase shift between the stators will produce a phase shift in the torque contributed from each stator.

This explanation does not attempt to provide any model for predicting a specific stator offset to create the optimal torque profile, but only suggests that the torque from each stator should be in complete misalignment, regardless of the stator angle that achieves this. This illustration implies that a misalignment of one-half commutation period is optimal, but the results from optimization suggest a different value for the stator offset, in either case of single-phase excitation or two-phase excitation. For single-phase excitation, the optimal stator offset is 15° , while for two-phase excitation, the optimal stator offset is 4° , compared with half of a commutation period being 7.5° . This discrepancy likely exists due to some coupling between the stators, as will be discussed later. Thus, the harmonic model cannot provide a complete model for why or how the torque profile is improved, although it is useful for building intuition.

4.2 Back emf analysis

Thanks to the separate windings on the inner and outer stator, the simulated back emf is available for separate analysis of the torque contributed from each winding.

The electrical power input is $P = i\varepsilon$, where ε is the back emf. If perfect energy conversion is assumed, the electrical power into the motor is equal to the electromagnetic power applied to the rotor. Each winding has its own back emf, and because the phase current is known, the electromagnetic power applied to the rotor from each winding is also known.

To derive torque from power, the power is divided by the rotor angular velocity: $T = P/\omega$. This estimate will not yield a perfect prediction for torque magnitude, but it will still provide useful insight to relative magnitude and phase of the torque profiles from each phase winding.

This torque estimate can be seen for single-phase operation of the motor in in Fig. 4.2 and 4.3 for the aligned and offset configuration, respectively. The top plot pane shows the

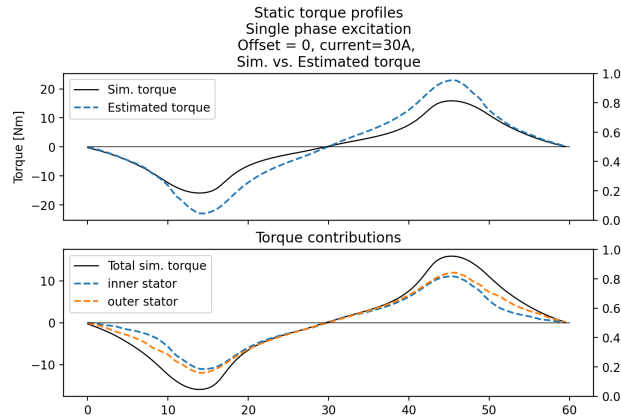


Figure 4.2. Estimated torque components from the back emf on the inner and outer stator for static excitation on phase A, in the aligned stator configuration. Note that the peaks in torque from the inner and outer stator are well aligned.

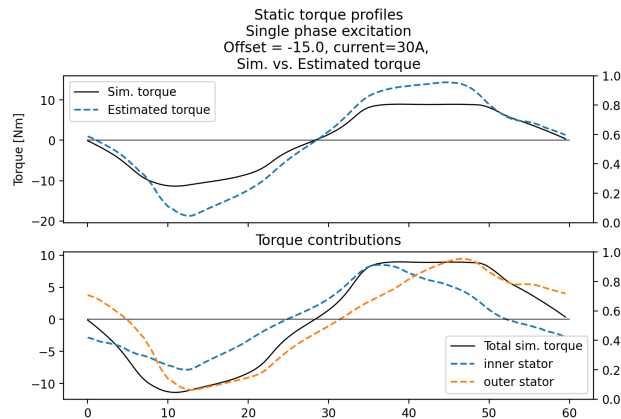


Figure 4.3. Estimated torque components from the back emf on the inner and outer stator for static excitation on phase A, in the offset stator configuration. Note the offset between the peaks of the torque contributions from each stator.

simulated torque against the estimated shaft torque, while the second plot pane shows the torque contributions from the inner and outer windings of phase A, separately. In the case that the stators are aligned, the torque contribution from the inner and outer stators are well-aligned, but in the case of offset stators, the torque contributions from each stator are offset. This phase shift will be measured and analyzed later.

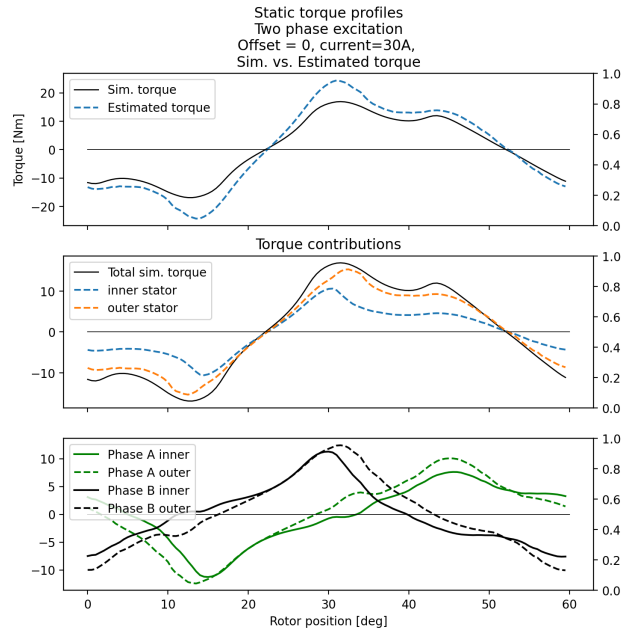


Figure 4.4. Estimated torque components from the back emf on the inner and outer stator for static excitation on phase A and B, in the aligned stator configuration.

This same torque component analysis can be applied to the motor in two phase operation. The torque components for two-phase operation can be seen in Fig. 4.4 and 4.5 for the aligned and offset configuration, respectively. The torque contribution of each stator does not change significantly when viewed as a whole, but a phase shift can be seen easily in the torque components when the four windings are plotted separately, in the lower panes.

To measure the phase shift of these torque contributions from each stator, a Fourier approximation is used with only the first harmonic component. This is equivalent to fitting a sine wave to the torque waveform, then extracting the phase information from that sine wave fit.

The phase information is analyzed for the torque contributions from each stator in the single-phase mode of operation. The phase analysis can be seen in Fig. 4.6 for the static torque profile, and in Fig. 4.7 for the commutated torque profile. In each case, the torque contributions are offset by about 7.5° for a stator offset of 15° .

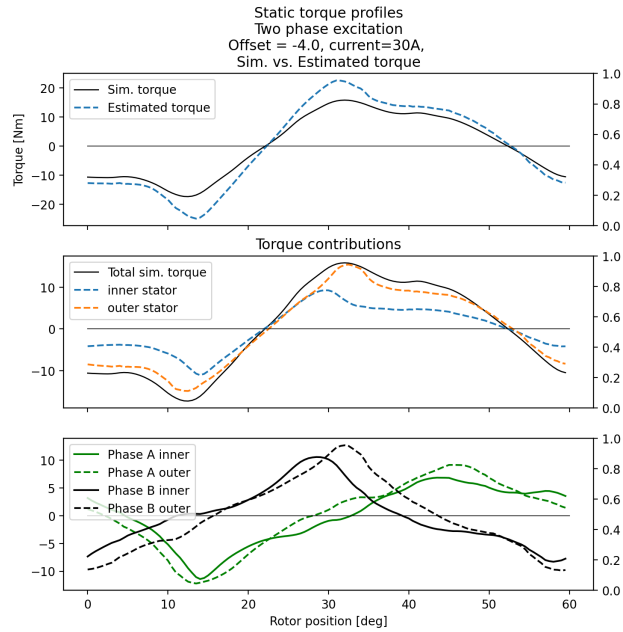


Figure 4.5. Estimated torque components from the back emf on the inner and outer stator for static excitation on phase A and B, in the offset stator configuration.

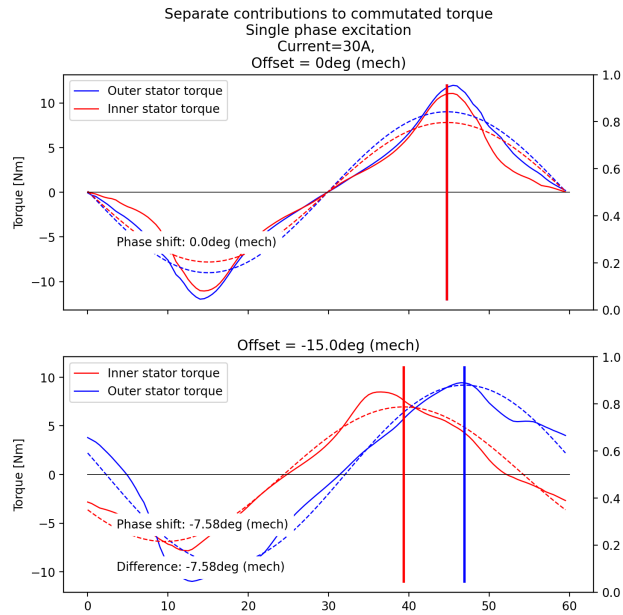


Figure 4.6. Static torque profile contributions from the inner and outer stator for single-phase excitations. The solid line is the torque estimate, while the dashed line represents a first-order Fourier series representation. The vertical bars represent the peaks of the sine fit.

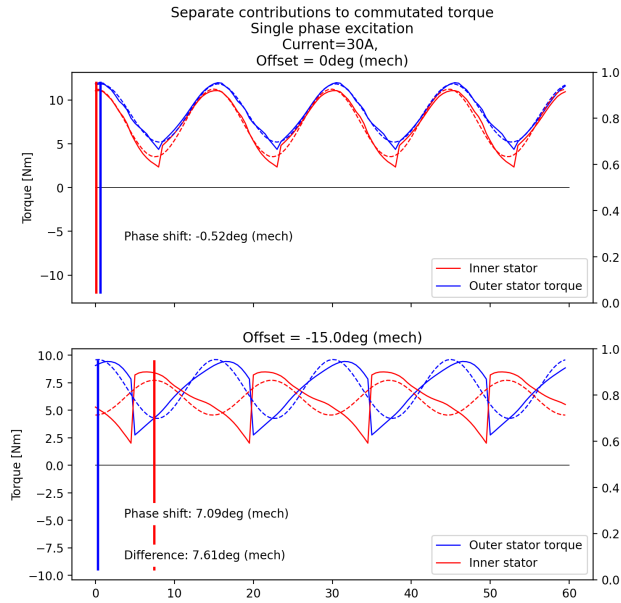


Figure 4.7. Commutated torque profile contributions from the inner and outer stator for single-phase excitations. The solid line is the torque estimate, while the dashed line represents a sine wave fit to the torque estimate. The vertical bars represent the peaks of the sine fit.

Next, the phase information is analyzed for the torque contributions from each stator in the two-phase mode of operation, combining phase A and B for inner and outer stator totals. This can be seen in Fig. 4.8 for the nominal and offset configurations. As mentioned previously, the torque contributions from do not show significant phase shifts between nominal and optimal configurations operated with two phases active.

If the phase information is analyzed for the commutated torque in two-phase excitation mode, the phase shift becomes slightly more pronounced, although is still a very small phase shift in comparison with the stator offset.

This phase information provides some insight to the mechanism by which the torque profile changes. In the single-phase mode of operation, the separate torque contributions show the largest phase shift relative to the stator offset. The torque phase shift is only about half of the stator offset however, showing a phase shift of 7.5° for a stator offset of

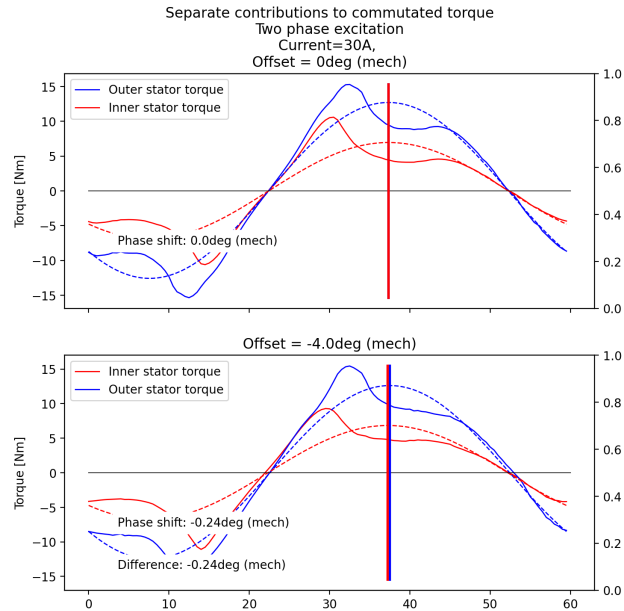


Figure 4.8. Static torque profile contributions from the inner and outer stator for two-phase excitations. The solid line is the torque estimate, while the dashed line represents a first-order Fourier series representation. The vertical bars represent the peaks of the sine fit

15°. This result implies that while the torque contributions do show a slight phase shift, the stators are not completely decoupled as previously postulated. The torque phase shift corresponds to one half of the stator offset, which implies that the torque is created primarily from a coupling between the inner and outer phases, and that the "center" of the torque can be described as originating from the "center" of the two windings, or half of the stator offset.

In the two-phase mode of operation, the phase shift of the torque contributions is even less pronounced than in the single-phase mode of operation. This implies that in two-phase mode, the torque is generated almost exclusively from coupling between all active phases, even more so than in single-phase operation.

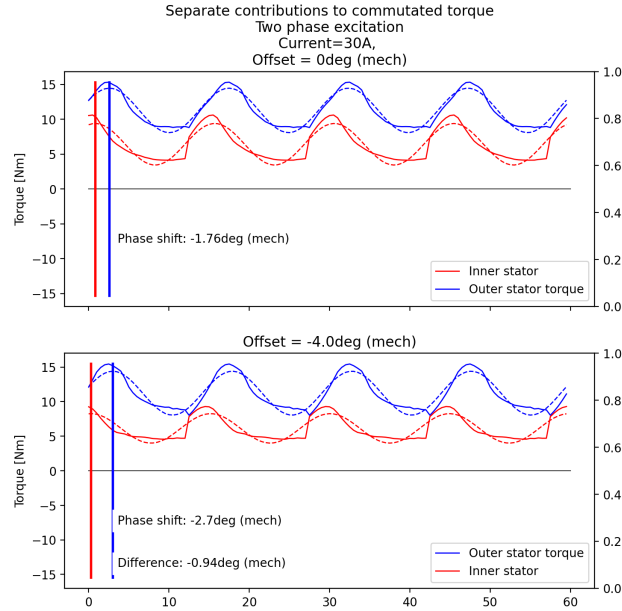


Figure 4.9. Commutated torque profile contributions from the inner and outer stator for two-phase excitations. The solid line is the torque estimate, while the dashed line represents a sine wave fit to the torque estimate. The vertical bars represent the peaks of the sine fit.

4.3 Inductance torque contributions

While the former explanation is able to describe the torque from each winding separately, it is unable to describe the torque from the interaction between windings. To describe such interactions, the torque from inductance data must be explored.

The torque in the motor will be created from the sum of several self inductance terms as well as from several mutual inductance terms. Because the windings are considered separately for the inner and outer stators, this yields a full inductance matrix of size 8. This means that the torque will be generated from 8 self-inductance terms which occur on the diagonal, and from $8(8 - 1)$ mutual inductance terms off the diagonal. Due to symmetry of the inductance terms above and below the diagonal ($L_{12} = L_{21}$), the number of mutual inductance terms is reduced to $\frac{8(8-1)}{2}$ but this still gives 28 mutual inductance terms, which is a bit unwieldy.

The final simplification is to reduce the dimension of the inductance matrix to only consider the phases which are active at a given time. For single-phase mode of operation, there are still two windings if the inner and outer stators are considered separately, which yields an inductance matrix L_2 with two self-inductances and one unique mutual inductance, as shown in eq. 4.1. For two-phase operation, there are four windings yielding an inductance matrix L_4 of size 4, with 6 unique mutual inductance terms, shown in eq. 4.2

$$L_2 = \begin{bmatrix} L_{11} & L_{12} \\ L_{21} & L_{22} \end{bmatrix} \quad (4.1)$$

$$L_4 = \begin{bmatrix} L_{11} & L_{12} & L_{13} & L_{14} \\ L_{21} & L_{22} & L_{23} & L_{24} \\ L_{31} & L_{32} & L_{33} & L_{34} \\ L_{41} & L_{42} & L_{43} & L_{44} \end{bmatrix} \quad (4.2)$$

The self-inductance torque is given in eq. 4.3, while the mutual torque from each mutual inductance term is given from eq. 4.4. Note that eq. 4.4 assumes that the lower inductance terms are neglected due to symmetry. If the upper and lower terms are both to be included explicitly, a $\frac{1}{2}$ term must be added to each mutual inductance torque.

$$T_{\text{self}} = \frac{1}{2} i_1^2 \frac{dL_{11}}{d\theta} \quad (4.3)$$

$$T_{\text{mutual}} = i_1 i_2 \frac{dL_{12}}{d\theta} \quad (4.4)$$

Because the self-inductance and mutual inductance are known for each winding, the torque contribution can be plotted separately for each torque component. This is shown in Fig. 4.10 for the single-phase mode.

For the single-phase torque, one noteworthy detail is the relative magnitude of the torques from the self-inductances and from the mutual inductance. The mutual torque contributes

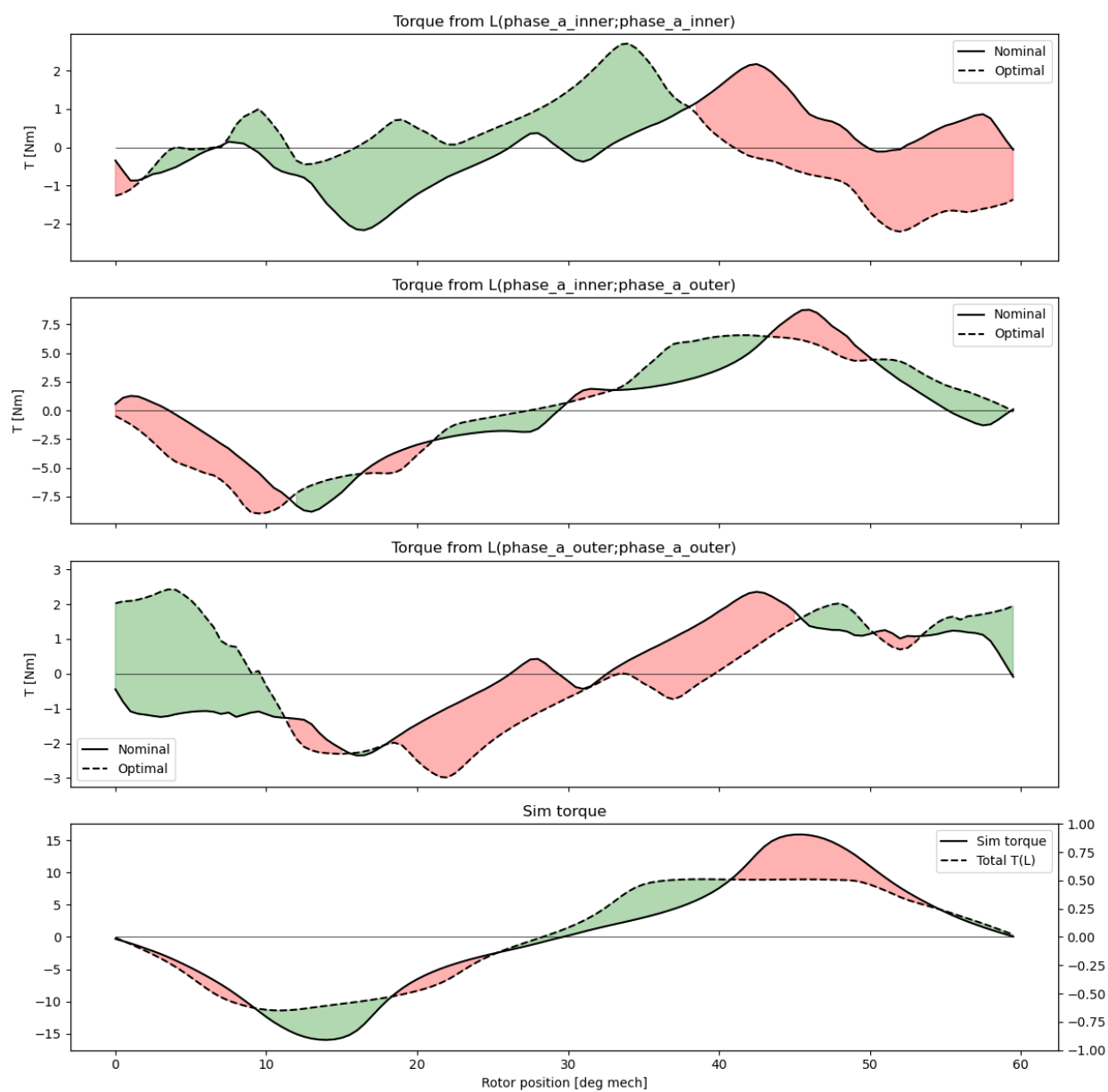


Figure 4.10. Torque contributions from the inductance matrix of the motor in single-phase mode. Green regions represent regions where the torque after optimization is greater than the original torque.

about half of the shaft torque, while each of the self-inductance torques provide about 25% each. The torque from the inner stator is shifted to the left by roughly 10 degrees, which is consistent with the mechanism of a stator phase shift causing a torque phase shift. The torque from the outer stator is also shifted, but it is shifted to the right by about the same amount. The mutual torque, in the region where the shaft torque is positive, is shifted to the left, but more importantly, is smoothed out significantly.

The large relative magnitude of the mutual torque, and the phase shift in the outer stator self-inductance torque, imply again that a large component of the torque in this motor is generated from the coupling effects between the inner and outer stators.

The same inductance component decomposition is applied to the motor in two-phase mode. As stated previously, this gives 4 self-inductance torques and 6 mutual inductance torques. This illustration is included as Fig. 4.11 for completeness, although it is not interpreted.

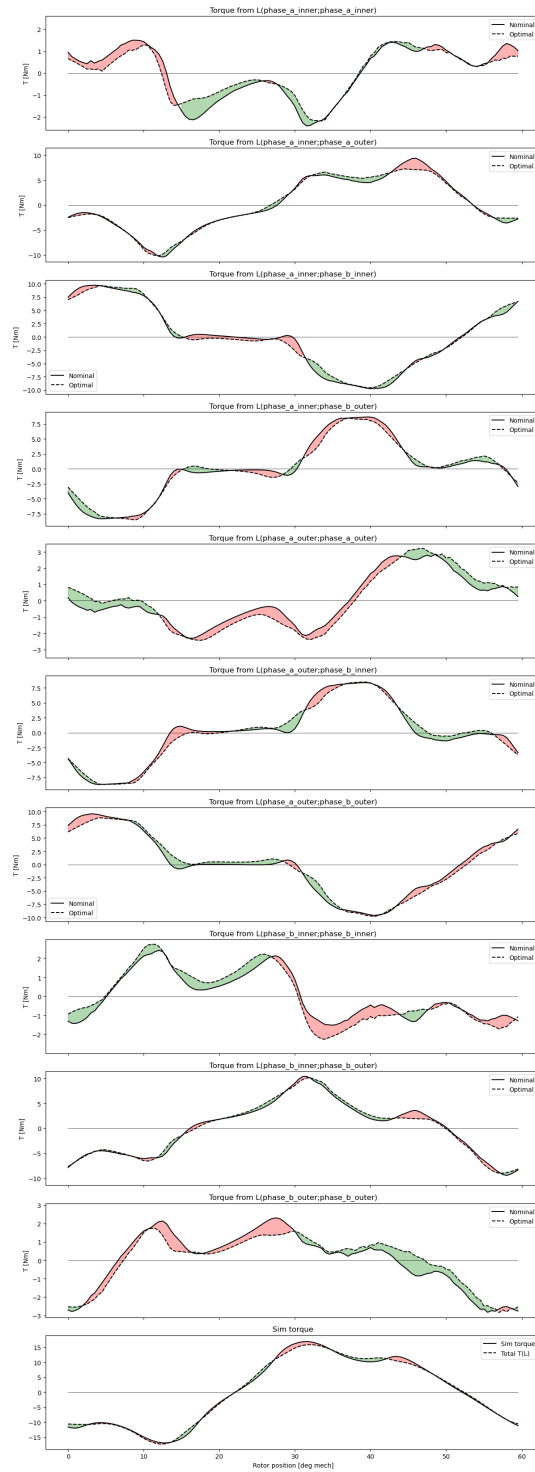


Figure 4.11. Torque contributions from the inductance matrix of the motor in two-phase mode. Green regions represent regions where the torque after optimization is greater than the original torque.

CHAPTER 5

CONCLUSION

At the beginning of this thesis, a question was posed: can the torque ripple in the DSSRM be reduced by misaligning the two stators, without significant penalty to the mean torque?

In the case of two phase excitation, the answer is a resounding yes. The optimal offset between stators was -4° , which is different from the nominal design with zero offset. The torque ripple was reduced by 36% in simulation with a drop in mean torque of 2%, and in experiment the results were even better. The experimental torque profile showed a drop in torque ripple of 54% with a net increase of torque by 2%.

In the case of single phase excitation, the answer is again yes, but with more nuance. The motor produced the best torque profile when the stators were offset by -15° , which is again different from the nominal motor and quite different from the optimal offset for the motor operated in two-phase excitation mode. The torque ripple was reduced in simulation from 90% in the case of the original design to 9% in the optimized design, for a 90% reduction. This reduction in torque ripple is a compelling result, even when it is considered alongside the 20% penalty in mean torque. For a switched reluctance motor, 9% torque ripple is a compelling result. Unfortunately due to time constraints, this result was not verified in experiment.

5.1 Future work

Some of the simplifications in this work lead directly to avenues for future investigation. The static torque profile is the only torque waveform considered in this work, but due to core losses and the phase current transient times in a motor operated at normal speeds, the optimal stator offset may change slightly in a real application. Similarly, the offset is only optimized for running the motor in saturated conditions. The results are slightly different for the motor in unsaturated conditions, but these results are not discussed.

In some of the static torque profiles, the single-phase torque has peaks that exceed the two-phase static torque profiles. With this in mind, there is likely room to improve the mean torque of this motor significantly by operating this motor with some phase overlap, but not total phase overlap, resulting in a hybrid of the one-phase and two-phase modes of operation. In other words, at some angular positions, the torque may be increased by removing excitation from one of the two active phases.

The optimization results for the motor in single-phase excitation provide a compelling reduction in torque ripple. It is expected that an even more compelling result would emerge from the combination of this offset method with the rotor shape contouring method in (Wang et al., 2015). Similarly, a small amount of current contouring has the potential to completely smooth out the rest of the torque pulsations.

REFERENCES

- Abbasian, M., B. Fahimi, and M. Moallem (2010). High torque double-stator switched reluctance machine for electric vehicle propulsion. In *2010 IEEE Vehicle Power and Propulsion Conference*, pp. 1–5.
- Abbasian, M., M. Moallem, and B. Fahimi (2010). Double-stator switched reluctance machines (dssrm): Fundamentals and magnetic force analysis. *IEEE Transactions on Energy Conversion* 25(3), 589–597.
- Brown, G., R. Jansen, and J. Trudell (2007, Jul). High specific power motors in ln2 and lh2.
- Carlson, W. B. (2013). *Tesla : inventor of the electrical age*. De Gruyter eBooks. Princeton, New Jersey: Princeton University Press.
- Hair, C., A. Parsapour, M. Moallem, and B. Fahimi (2019). On the effects of mechanical offset between inner and outer stator in a 4-phase double stator switched reluctance machine. In *2019 IEEE International Electric Machines Drives Conference (IEMDC)*, pp. 591–596.
- Hirayama, T. and S. Kawabata (2017). Study on design method for thrust ripple reduction of double-sided linear switched reluctance motor. In *2017 11th International Symposium on Linear Drives for Industry Applications (LDIA)*, pp. 1–5.
- Iwamuro, N. and T. Laska (2017). IGBT history, state-of-the-art, and future prospects. *IEEE Transactions on Electron Devices* 64(3), 741–752.
- Lee, C. H., J. L. Kirtley, Jr., and M. Angle (2017). Switched reluctance motor drives for hybrid electric vehicles. In A. Tahour and A. G. Aissaoui (Eds.), *Switched Reluctance Motor*, Chapter 6. Rijeka: IntechOpen.
- Lee, C. H. T., K. T. Chau, C. Liu, T. W. Ching, and F. Li (2014). Mechanical offset for torque ripple reduction for magnetless double-stator doubly salient machine. *IEEE Transactions on Magnetics* 50(11), 1–4.
- Ma, J., R. Qu, and J. Li (2014). Optimal design of axial flux switched reluctance motor for electric vehicle application. In *2014 17th International Conference on Electrical Machines and Systems (ICEMS)*, pp. 1860–1865.
- Maharjan, L., E. Bostanci, S. Wang, E. Cosoroaba, W. Cai, F. Yi, P. Shamsi, W. Wang, L. Gu, M. Luo, N. Arbab Rahman, M. McDonough, C. Lin, J. Hearron, C. Caicedo Narvaez, M. Wu, A. Hassanpour Isfahani, Y. Li, G. Rao, M. Moallem, P. T. Balsara, and B. Fahimi (2018). Comprehensive report on design and development of a 100-kw dssrm. *IEEE Transactions on Transportation Electrification* 4(4), 835–856.
- Miller, T. J. E. (2001). *Electronic control of switched reluctance machines*. Newnes.

- Rahman, M. A., A. Chiba, and T. Fukao (2004). Super high speed electrical machines - summary. In *IEEE Power Engineering Society General Meeting, 2004.*, pp. 1272–1275 Vol.2.
- Richter, E. (1988). High temperature, lightweight, switched reluctance motors and generators for future aircraft engine applications. In *1988 American Control Conference*, pp. 1846–1851.
- Sebastian, T. (1995). Temperature effects on torque production and efficiency of pm motors using ndfeb magnets. *IEEE Transactions on Industry Applications* 31(2), 353–357.
- Wang, W., M. Luo, E. Cosoroaba, B. Fahimi, and M. Kiani (2015). Rotor shape investigation and optimization of double stator switched reluctance machine. *IEEE Transactions on Magnetics* 51(3), 1–4.

BIOGRAPHICAL SKETCH

Colbey Hair was born in Fort Worth, Texas. He attended Arlington High School, graduating in the class of 2012. He studied physics at The University of Texas at Arlington, tutoring calculus and then physics from his sophomore year until graduation. After taking a year off of school, he began studies for a Master of Science in Electrical Engineering at The University of Texas at Dallas, affiliated with the Renewable Energy and Vehicular Technology lab, where he focused on power electronics and electric machines. Between his third and fourth semesters of study, he took an educational hiatus to intern at NASA Goddard Space Flight Center in the summer of 2019, and then at Tesla from August 2019 to August 2020. After graduation, Colbey intends to take a role in electrical research and development in the aerospace industry.

CURRICULUM VITAE

Colbey N. Hair

December 1, 2020

Contact Information:

Department of Electrical and Computer Engineering
The University of Texas at Dallas
800 W. Campbell Rd.
Richardson, TX 75080-3021, U.S.A. Email: colbey.hair@gmail.com

Educational History:

B.S., Physical Sciences, minor in Mathematics, The University of Texas at Arlington, 2016

Employment History:

Electronic Hardware Design Intern, Tesla, Inc., June 2020 –August 2020
Power Electronics Controls Intern, Tesla, Inc., August 2020 –June 2020
Electromechanical Engineering Intern, NASA, July 2019 –August 2019
Audiovisual Technician, self-employed, October 2016 –December 2018,
Physics Tutor, The University of Texas at Arlington, August 2015 –May 2016
Calculus Tutor, The University of Texas at Arlington, August 2013 –May 2014
Automotive Collision Repair Apprentice, Texas Quality Collision Center, May 2012 - August 2012

Professional Recognitions and Honors:

Graduated *cum laude*, The University of Texas at Arlington, 2016
Presidential Award Scholarship, The University of Texas at Arlington, 2012